
# ADDIS ABABA UNIVERSITY

# ADDIS ABABA INSTITUTE OF TECHNOLOGY

# SCHOOL OF MULTIDISCIPLINARY ENGINEERING

# CENTER FOR MATERIALS ENGINEERING

# MASTER THESIS

## First-principles study of van der Waals heterostructures of MoSeTe/ZnO for investigating photocatalytic water-splitting and photovoltaic applications

**By: Derese Abraham Solomon**

**A Thesis Submitted to the Center for Materials Engineering in Partial Fulfillment of the Requirements for the Degree of Science in Materials Engineering**

June 2023
Ethiopia

This is to certify that the thesis entitled "**First-principles study of van der Waals heterostructures of MoSeTe /ZnO for investigating photocatalytic water-splitting and photovoltaic applications.**" is prepared and submitted by Derese Abraham in partial fulfillment of the requirements of the degree of Master of Science in Materials Engineering complies with the regulation of the university and meet the accepted standards concerning originality and quality

Approval by the Board of Examiners

| | Signature | Date |
|---|---|---|
| Georgis Alene (Dr) | _____ | _____ |
| Advisor | | |
| Kingsly Obodo(Dr) | _____ | _____ |
| Co. Advisor | | |
| Anteneh Marelign (Dr) | _____ | _____ |
| Internal Examiner | | |
| Yedilfana Setarge (Dr) | _____ | _____ |
| External Examiner | | |

## DECLARATION

I hereby declare that the work that is being presented in this thesis entitled “First-principles study of van der Waals heterostructures of MoSeTe/ZnO for investigating photocatalytic water-splitting and photovoltaic applications.” is new work of my own, has not been presented for a degree of any other university and all the resource materials used for this thesis have been accordingly acknowledged.

Name: Derese Abraham Solomon signature Date

_____ _____

This is to certify that the above declaration made by the candidate is correct to the best of our knowledge and it has been submitted for the examination with our approval as university advisor.

Goergis Alene Asres (Dr) signature Date

Advisor _____ _____

## ACKNOWLEDGMENT

I want to start by giving God praise for enabling me to finish both my thesis and my master's degree. Then, I want to sincerely thank my advisor, Dr. Georgies Alene, for his inspiration, unwavering support, and direction as I worked on my MSc thesis. In addition to my advisor, I would like to express my gratitude to Dr. Kingsley Obodo for providing the essential resources and ongoing support, without which I could not have finished this thesis. I was able to take advantage of numerous opportunities to work with others and learn how to use new materials thanks to his assistance. Finally, I would like to express my gratitude to my family and friends who greatly assisted me in completing my thesis. You are always there, not only for this work but all the time

## ABSTRACT

*Two-dimensional (2D) heterostructures have allowed for the development of novel properties with interesting applications in photocatalytic water splitting and optoelectronic devices. Electronic properties of ZnO and Janus MoSeTe monolayers were investigated using density functional theory (DFT)-based first-principles calculations, and depending on the lattice mismatch, layered 2D MoSeTe/ZnO heterostructures were produced. In this study, the first-principles van der Waals corrected density functional theory calculations were also performed on ABI_Se, ABI_Te, and ABII_Te heterostructure.Out of eight basic stacking patterns of the ZnO/MoSeTe hetero-bilayer designed, the ABII-Te stacking mode was a more stable stacking type due to the small lattice mismatch and the binding energy. The result showed that the band alignment for ABI_Se, ABI_Te, and ABII_Te was done on the electrical band structure and band edge positions, and confirmed type two band alignment. In addition, the ABI_Se, ABI_Te, and ABII_Te configurations of ZnO/MoSeTe vdW heterostructures are indirect band gap semiconductors. The investigated 2D ZnO/MoSeTe heterostructures have an acceptable band gap for solar applications, according to a first-principles study. The power conversion efficiency of ZnO/MoSeTe heterostructure is computed, and the results exhibit ABI_Se, ABI_Te, and ABII_Te stacking orientations have high efficiency with values of 22.26%, 22.31%and22.17%, respectively. Therefore, our findings show the heterostructures have reasonable band gaps and high PCE, and exhibit type-II band alignment, which are suitable candidates for solar cell application. Furthermore, for full water splitting heterostructures cannot satisfy the band edge requirements; however, the heterostructures are a good photocatalyst for the hydrogen evolution reaction. The heterostructure's ability to split water more effectively can be improved by moving the band edges position using strain and doping.*



**Keywords:** MoSeTe/ZnO heterostructures, DFT, band alignment, band gap, power conversion efficiency, photovoltaics, photocatalyst, water splitting

## TABLE OF CONTENTS

## LIST OF FIGURES

## LIST OF TABLE

## LIST OF ACRONYMS

| | |
|---|---|
| TMD | Transition metal dichalcogenide |
| 2D | Two-dimensional |
| JTMDs | Janus transitional metal dichalcogenide |
| DFT | Density-functional theory |
| PDOS | Partial density of state |
| eV | Electron Volt |
| Eb | Binding energy |
| LDA | Local-density approximation |
| PAW | Projected augmented wave |
| GGA | Generalized Gradient Approximation |
| HF | Hartree-Fock |
| MoSeTe | Molybdenum selenide telluride |
| ZnO | Zinc Oxide |
| $MoS_2$ | Molybdenum disulfide |
| MoSSe | Molybdenum disulfide selenide |
| WSSe | Tungestundisulfide selenide |
| PV | Photovoltaic |
| vdWH | van der Waals heterostructure |
| CBM | Conduction band minimum |
| VBM | Valence band maximum |
| XC | Exchange correlation |
| PBE | Perdew–Burke–Ernzerhof |
| HSE | Heyd-Scuseria-Ernzerhof |
| PCE | Power conversion efficiency |

# CHAPTER ONE: INTRODUCTION

## 1.1. BACKGROUND OF THE STUDY

The production of energy from renewable resources is perpetual. The availability of these resources is either unbounded in time or their rate of replenishment is faster than that of their rate of consumption. Non-renewable energy sources and those that depend on fossil fuels are frequently contrasted. Fossil fuel stocks such as coal, oil, and natural gas are depletable and not replenishable on a human time scale.

The future of the world will be significantly influenced by renewable energy resources. Renewable energy is produced from natural resources that replenish more quickly than they are used up. The sun, water, and wind are a few such sources that are constantly supplied. We have access to a wide variety of renewable energy sources[1]. Renewable energy sources that fulfill domestic energy needs possess the capability to offer energy services while producing little to no air pollutants or greenhouse gas emissions[2].

Renewable energy sources include photovoltaic electric current generation and the photocatalytic synthesis of hydrogen from water splitting[3]. The sources of solar energy can be repeatedly utilized for energy production purposes[2]. Solar energy, which consists of "photons," is converted into electricity by solar cells (SCs) also known as photovoltaics or "PVs" so that electrical loads can be powered. SCs are formed by combining layers of p-type and n-type semiconductors, one layer can absorb electrons (p-type), while the other can donate electrons (n-type).

Solar cooking is the most feasible and straightforward application of solar energy. Solar energy has the potential to emerge as a leading energy source for cooking, serving as a viable alternative[2].

Since the study detailed by Fujishima and Honda in 1972 using a rutile titanium dioxide (TiO2) anode paired with a platinum cathode for photo-assisted electrolytic water splitting, numerous attempts have been made to create efficient heterogeneous water-splitting systems[4]. By exposing semiconductors to light, electrons (or holes) are generated in the conduction (or valence) band, which, in turn, facilitates the reduction (or oxidation) of water molecules, thereby resulting in the complete separation of water into hydrogen and oxygen gases. The locations of a semiconductor'

band boundaries are another crucial condition for photocatalytic water-splitting events. Recent discoveries in 2D materials, in particular, hold significant promise for overcoming current material limitations in energy applications due to their remarkable mechanical, chemical, electrical, optical, and magnetic properties[5]. The specific characteristics of 2D structures, such as form, surface charge, anisotropy, and adaptability, increase their potential applications.

The ZnO-Janus heterostructures have shown potential for energy-related applications such as solar cells and catalysis. The unique Janus structure of ( MoSSe and WSSe ) heterostructures leads to exceptional electronic and optical properties, which can be tuned by controlling the number of layers and the stacking sequence of the constituent materials. The MoSSe/ZnO and WSSe/ZnO heterostructures offer a promising avenue for the development of advanced energy-related applications.

Extensive research has been conducted on ZnO due to its unique properties, which make it a promising candidate for use in solar cells and water-splitting applications[6].According to a study by Zhang et al. ZnO is a promising material for solar cells and water-splitting technologies due to its high electron mobility, wide band gap, and outstanding stability[7]. The study highlights the importance of optimizing the fabrication and design of ZnO-based devices to achieve maximum efficiency, but overall, the results suggest that ZnO has great potential for use in renewable energy applications.

## 1.2. STATEMENT OF THE PROBLEM

Our primary sources for producing power are coal and oil, both of which have negative environmental and air quality effects, are scarce resources, and pose a threat to plant and animal health. Consequently, the increasing interest in and activity surrounding the creation and use of renewable energy sources. For instance, the development of effective motors, solar PVs, hydrogen storage, and better batteries all present opportunities for the prospective wide-scale deployment of innovative materials [8]. The need for improved functionality and efficiency, and the requirement to discover alternatives for raw materials that are in limited supply or which have negative effects on human health as well as on the environment are just a few of the drivers that lead to the development of novel materials. The growth of photovoltaics, photocatalytic water-splitting, and fuel cells as well as the increased efficiency and functionality of innovative materials, can produce real environmental advantages [8]. Computational screening of novel materials based on two-dimensional JTMDs for water splitting and solar photovoltaic (PV) technologies is the main topic of this study. Because of their excellent absorption of a photon and electronic transport abilities, atomically thin 2D stacked JTMD semiconductor materials offer great potential. However, in the range of visible light irradiation, PVs and photocatalyst-efficient materials are the key issues. To develop a photocatalyst and photovoltaic system that can effectively utilize visible light, it is necessary to carry out appropriate band engineering to match the band gap of the prospective photocatalyst.

The utilization of ZnO and MoSeTe in photovoltaic and photocatalyst applications provides several advantages. The wide band gap of ZnO allows for efficient absorption of high-energy photons, while the band gap of MoSeTe can be adjusted by varying the thickness of the material, making it tunable. The abundance and affordability of ZnO make it an attractive material for large-scale production. MoSeTe can be easily integrated with other materials to create heterostructures that demonstrate enhanced performance in photovoltaic and photocatalytic applications. In this study, we chose to design vdW heterostructures for photovoltaic devices and photocatalysts with the potential to achieve higher efficiency based on the remarkable properties of ZnO and MoSeTe monolayers.

## 1.3. THE OBJECTIVE

### 1.3.1. GENERAL OBJECTIVE

To investigate 2D vdW heterostructures of MoSeTe/ZnO for high-performance photovoltaic and photocatalyst water-splitting applications using first-principles calculations.

### 1.3.2. SPECIFIC OBJECTIVES

- To optimize the geometry of MoSeTe and ZnO monolayers, and van der Waals (vdW) heterostructures of ZnO/MoSeTe
- To design different stacking of 2D MoSeTe/ZnO heterostructures.
- To analyze the electronic properties of ZnO and MoSeTe monolayers, and ZnO/MoSeTe heterostructures.
- To assess the band alignment and PCE of MoSeTe/ZnO vdW heterostructures for water splitting and solar cells respectively.

## 1.4. SIGNIFICANCE

The study is important in a variety of ways. Renewable energy is the main viable choice to fossil fuels for meeting the present energy demand because it has an unlimited supply and is environmentally friendly. The use of solar cells or photocatalysts to split water into oxygen and hydrogen while increasing their efficiency has drawn much interest in renewable energy technology. The government and society will focus on and switch to using other alternative sources of energy as a result of enhancing the overall efficiency of energy conversion and storage, keeping and saving our environment.

The study's findings can be applied to the hydrogen and solar cell manufacturing industries. Additionally, it is preferable to combine theoretical modeling features with experimental works to comprehend and research their photocatalytic effectiveness and electronic applications.

## 1.5. THESIS OUTLINE

The rest of the thesis is structured as follows.

An overview of the related literature on 2D vdW heterostructures, with a focus on Janus transitional metal dichalcogenide materials, is presented in Chapter 2. The key points of the theoretical and technical elements of the computational methods taken into consideration in this work are covered in Chapter 3. Based on the aforementioned particular objectives that were described in Chapter 1, Chapter 4 shows the key findings and a discussion of the qualitative and quantitative components of the thesis. Finally, the summary and upcoming work for the thesis will be connected to Chapter 5.

# CHAPTER TWO: RELATED LITERATURE REVIEW

## 2.1. TWO-DIMENSIONAL MATERIALS

A huge deal of interest has been generated in 2D materials and their newly discovered physicochemical properties since the finding and separation of graphene in 2004 [9]. High charge migration rates and massless carrier mobility are all characteristics of graphene. However, the use of pristine graphene in nanoscale electrical devices is constrained by the lack of a band gap. This drawback has spurred substantial studies into how to increase graphene's band gap while preserving or barely affecting its superior charge-transport capabilities.

Controlling the electrical characteristics of graphene can be accomplished by manipulating its structure, for example by creating nanoribbons from pristine layers. Unfortunately, the removal of the Dirac cone and scattering effects can cause a considerable reduction in the carrier mobility of graphene nanoribbons compared to their pure counterpart [10–12]. For instance, the charge-carrier mobility in sub-10nm graphene nanoribbon transistors with field effect has been demonstrated to decline to less than 200 $cm^2V^{-1}s^{-1}$ given the lowered widths required to open a sufficiently wide band gap in these devices [13]. Although the placement of the new heteroatoms nearly invariably necessitates the introduction of a carrier recombination center, doping can also be useful in modifying the electronic characteristics of graphene.

Finding graphene analogs is an intriguing path that has attracted more research attention[14–16]. Because of their compositional flexibility and consequent tunability, TMDs, the prototypical class of graphene analogs, have drawn much attention. It is possible to design and create a wide range of TMD structures $MX_2$ (M = Nb, Mo, and W; X = S, Te, and Se) with composition-configurable band gap and transport characteristics[17,18]. Single-layer MoS2, a semiconductor with a band gap of around 1.9 eV[19], is considered to be a good option for field-effect transistors with an on/off ratio of greater than 10[16,20].However, it has been discovered that a suspended $MoS_2$ sheet has carrier mobility in the range of 0.5-3 $cm^2$ $V^{-1}s^{-1}$[21], and is linked to low device efficiency[22]. More research has demonstrated that improving the electron or hole mobility of $MoS_2$ until 200 cm2 V-1s-1[23,24] which can be potted in MoS2 armchair nanoribbons, can be accomplished by eliminating adsorbate impurities or placing on top of high-dielectric layer[25].

However, the variety of TMD structures that are feasible allows for various electronic structures ranging from metallic (such as NbS2) to semiconducting (such as $MoS_2$)

## 2.2. THE RISE OF 2D JANUS TRANSITIONAL METAL DICHALCOGENIDE MATERIALS

From a theoretical perspective, Cheng et al. were the first to anticipate a new Janus MXY(M = W, Mo; X Y = S, Te, Se)[26]. These researchers used simulations to demonstrate that the spin splitting in these polar TMDs is caused by the interaction of spin-orbital phenomenon[27]. After several years of work, experimentalists were able to prepare and characterize their particular Janus family, such as MoSSe[28]. The breaking out-of-plane structural symmetry of $MoS_2$ produces the Janus MoSSe monolayer[29,30]. In the direction opposite the MoSSe plane[31–33], an intrinsic electrostatic dipole was found, in contrast to conventional TMDs[34,35].

Theoretical findings show that the carrier mobility of the Janus MoSSe monolayer is 157 cm2 V-1s-1 for holes and 74 cm2 V-1s-1 for electrons. Furthermore, by adjusting the layer thickness and resulting perpendicular dipole, the electron and hole mobility can be easily modified[34]. Along with their tunable electrical properties, Janus structures were found to considerably improve the piezo-electric connected to the inherent dipole vertical to the planar structure by Guo et al.[36].

To the advantage of photocatalytic reactivity, intrinsic properties create an integrated electric field that in turn makes it easier to separate photogenerated charge carriers[37,38]. The MoSSe sheet may be a possible water-splitting photocatalyst with extensive solar light absorption and delayed electron-hole recombination, according to Ma et al.[39] data based on HSE06 calculations. A few layers of MoSSe can work well for visible light range water splitting, according to Guan *et al.*[40]. These findings have prompted additional research on photocatalytic water splitting.

The electronic structure, band gap, redox potentials, and carrier separation processes of Janus such asMoXY (X, Y = O, S, Se, and Te) [41], PtSSe[42], and $XM_2Y$ (X, Y = S, Se, Te; M = Ga, In) systems[43], were systematically studied via simulation. The calculations imply that the Janus materials under consideration might function as effective photocatalysts for water splitting. Janus materials have characteristics that can be additionally altered by doping, thickness, strain, and other factors, among others[44,45]. The fact that this field of study is still in its infancy inspires more computational and experimental study.

## 2.3. STRUCTURES

### 2.3.1. CRYSTAL STRUCTURES

Lu et al. [28] recently achieved the out-of-plane structural symmetry breaking of single-layer MoS2 by combining chemical vapor deposition, H2 plasma stripping, and Se-selective thermal vaporization to produce MoSSe monolayers. By using this technique, it is possible to transform the common TMD $MX_2$ (M = W, Mo; X = S, O, Te, Se) into its Janus MXY equivalent, which has Y and X as illustrated in Fig. 1.

The single-layer TMD $MX_2$ has a hexagonal structure, similar to graphene. The TMDs are composed of three different atomic layers organized in an X-M-X pattern. Practical and computational studies have revealed that Janus TMD MXY has many space groups. Despite having different atomic structures, several JMTDs, like 1-H and 1-T phases depicted in Figure 1 (a and b), possess identical P3M1 (C3V-1) groups. The X atom in the upper layer of the 1-H phase is directly on top of the Y atom in the lower layer. The X and Y atoms are both threefold coordinated, but the M atom is sixfold coordinated. The X atom in the top layer of the 1-T phase is instead positioned in the middle of the hexagonal ring of the Y atoms as a result of the translation of the X or Y atoms along the plane. The 1-T phase is metastable compared to the 1-H phase which can be created experimentally by extreme temperature treatment[46].

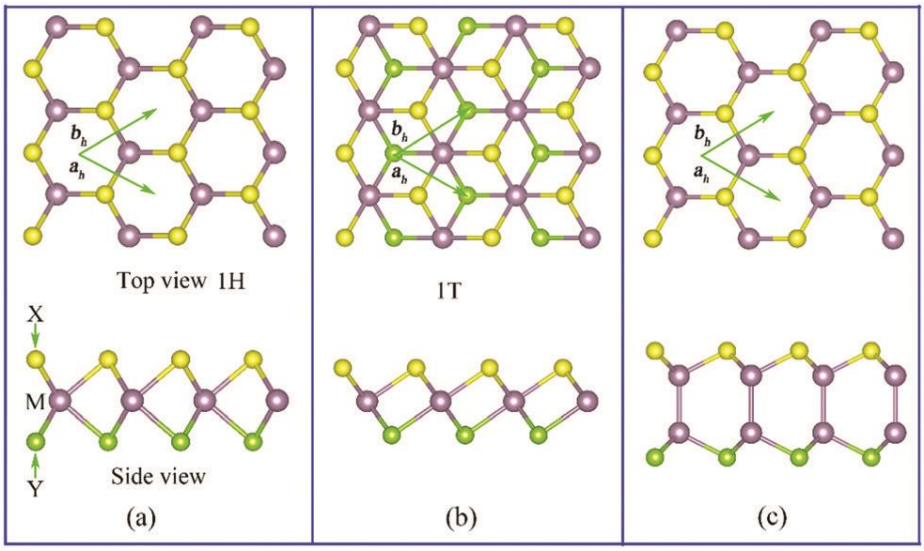


Figure 1: The atomic structures of Janus TMD low-dimensional potential phases. (a) MXY monolayers in their 1-H phase. (b) The 1-T phase of MXY monolayers. (c) Monolayers made of

Group-III Janus $M_2XY$ or $MM^0XY$ (M, $M^0$ = In, Ga; X, Y = S, Te, Se). The upper and lower panels, respectively, exhibit stacking configurations of the Janus materials. The primitive cell vectors ($a_h$and $b_h$) are designated by green arrows. The colors green and yellow represent the Y and X atoms, respectively. The color of the M ($M^0$) atoms is mauve[47].

Group-III monochalcogenides MX, including GaS, can have a hexagonal shape with symmetry group P3M1. This is in addition to the aforementioned JTMDs. The X atoms are three-fold coordinated, similar to TMDs.The bottom X atoms of monolayer MX compounds must be swapped out for Y atoms to produce $M_2XY$ monolayers to build Janus structures ( Fig. 4(c)).

To design $MM^0XY$ monolayers, the M atoms in the Janus $M_2XY$ system can be replaced by hetero-metal atoms ($M^0$). Guo et al.[36] produced the Janus monolayers $Ga_2SSe$, $Ga_2STe$, $Ga_2SeTe$, $In_2SSe$, $In_2STe$, $Ga_2SeTe$, $GaInS_2$, $GaInSe_2$, and GaInTe in this way. The two forms of Janus structures that exhibit broken inversion and mirror symmetries are $M_2XY$ (M = In, Ga; X, Y = Se, S, Te) and $MM^0XY$ (M, $M^0$= In, Ga; X, Y= Se, S, Te).

### 2.3.2. JMTD MONOLAYERS

MoSSe and WSSe are 2D Janus monolayer materials that have recently been successfully prepared experimentally by several groups[29,48,49]. These materials have been proven to contain an intrinsic electrostatic dipole moment, which is desirable for nanoscale electronic devices[50]. The out-of-plane structural symmetry of the pure $MX_2$ parent compound can be broken to produce the Janus MXY monolayer, as depicted in Figure 5 ((a) and (b)). To create a Janus MoSSe sheet, one S atom from $MoS_2$ are switched out for Se atoms while still preserving the hexagonal structure.

The relaxed lattice parameter (3.21 vs. 3.19) and Mo-S bond length (2.42 vs. 2.41) in MoSSe and MoS2 are comparable, according to the DFT findings at the PBE level [34]. Figure 5(c) shows that the Janus MoSSe monolayer has a lower PBE-DFT band gap of 1.66 eV than $MoS_2$ (1.78 eV). According to the TDOS and PDOS for this material, Mo (4)d electrons dominate the conduction band minimum (CBM) for MoSSe. However, the principal source of the VBM is states produced by the rehybridization of the Mo-4d, S-3p, and Se-4p electrons. The PBE function typically decreases the bandwidth for semiconductors. An enhanced band gap of 2.01 eV for the Janus MoSSe is predicted based on HSE functional studies that are more precise than expected.

Other Janus TMD monolayers have also been suggested in addition to MoSSe based on simulations. For instance, Xia et al.[51] applied first-principles simulations to study the Janus WSSe monolayer. Their analysis of the system's phonon dispersion revealed no negative frequencies, indicating that Janus WSSe monolayers are dynamically stable. Band gaps of approximately 1.70 eV (PBE) and 2.18 eV (HSE), which are a little greater than those for the MoSSe monolayer at the same level of theory, are revealed by the characterization of the electronic structure of Janus WSSe. Additionally, it appears that the Te atom replacement for the Se atoms dramatically lowers the HSE estimated band distance of WSSe and WSTe from 2.18 eV to 1.71 eV, respectively.

Other types of Group III Janus chalcogenide monolayer structures, including WSSe and MoSSe, have been investigated through simulations. $In_2SeTe$, $Ga_2STe$, $Ga_2SeTe$, $Ga_2SSe$, $In_2SSe$, $In_2STe$, $GaInS_2$, $GaInTe_2$, and$GaInSe_2$ were the systems that Guo et al.[36] concentrated on. The authors discovered appealing features for use in piezoelectric devices by discovering (PBE-DFT) band gaps for these systems in the range of 0.89-2.03 eV.

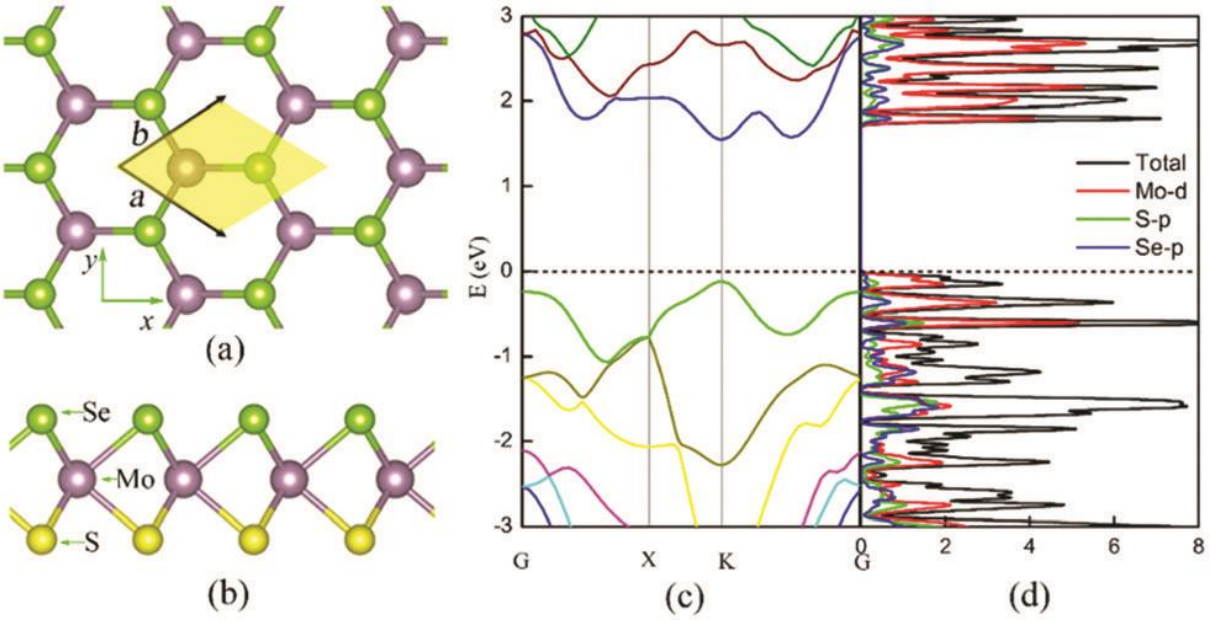


Figure 2: The Janus MoSSe monolayer's atomic and electronic structures[34].

### 2.3.3. JTMD MULTILAYERS

It is known that a material's electrical and structural characteristics can be quite responsive to its nanostructuring. Therefore, it is intriguing to investigate and measure the impacts that various JMTD configurations can have on the characteristics of the composite nanostructured material[52,53]. The MoSSe sheet has different atoms on either side, which allows for the formation of bilayers with three distinct interfaces: SMoSe/SMoSe, SeMoS/SMoS, and SMoSe/SeMoS. Additionally, MoSSe bilayers can be stacked in different ways, as indicated in Fig. 4, where the patterns are denoted by the letters AA-, AB-, and AC-, depending on how one layer is translated relative to the next.

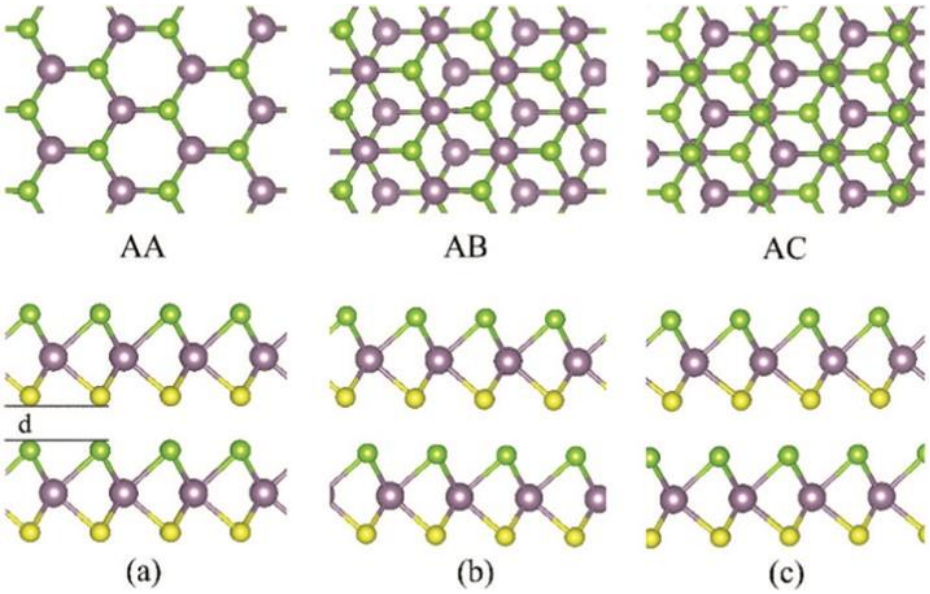


Figure 3: The different MoSSe bilayer stacking types. The upper and bottom panels, respectively, report top and side views. identical atom-color labeling as in Figure 2[54].

The simulations show that, despite the interface mode, AC-stacking has the lowest formation energy, indicating that it is the more stable stacking type with a Se/S interlayer distance of 2.91Å. The AC-stacked MoSSe bilayer is a 0.96 eV indirect-gap semiconductor, according to PBE-DFT simulations[34]. To obtain more accurate results, Ji et al.[41] investigated the Janus MoSSe bilayer's electrical structure at the HSE06 level. They came up with a direct band gap estimate of 1.98 eV, which was 0.4 eV higher than the PBE result[41]. The band gap of these systems narrows with an increase in the number of layers for thicker Janus MoSSe multi-layers.

The band gap of Janus MoSSe was discovered by scientists to fall to 1.53 eV, 0.75 eV,0.37 eV, and 0.16 eV for the bilayer, tri-layer, four-layers, and five-layers, respectively. The electronic characteristics of Janus MoSSe multilayers have also been investigated using beyond-DFT strategies such as the G0 W0 technique. Guan et al.[40] discovered that a stable MoSSe bilayer has a band gap of approximately 1.47 eV, making it an indirect semiconductor. Notably, the indirect band gap of the multilayer MoSSe drops monotonically as the number of layers grows because of the interactions between the various layers, which is qualitatively consistent with the HSE06-DFT results[41].

### 2.3.4. JTMD HETEROSTRUCTURES

Interlayer interactions and quantum confinement effects have a big impact on multilayer Janus materials' structural and electrical properties. The assembly of heterogeneous multilayers, or heterostructures, results in interface-specific interactions, which may allow for the coexistence of various emerging effects. In contrast, the similar Janus multilayers, are invariably characterized by the same interactions at the interface between the same layers. The increased interest in heterostructures constructed of various Janus TMDs is driven by these factors.

Based on the geometrical properties of the interfaces, Janus TMD heterostructures can be classified into two groups: out-of-plane and in-plane longitudinal heterostructures with the component bonding perpendicular to the 2D plane of the sheets[55]. One heterostructure can be composed of two different Janus monolayers, such as WSSe and MoSSe, and the other can be constructed from Janus monolayers such as MoSSe or WSSe, with a typical 2D material, such as $MoS_2$, GaN, graphene, etc.

At a noncollinear PBE level, Li et al.[56] investigated several heterostructures built by merging MoSSe and WSSe Janus monolayers. They discovered that the improved out-of-plane electric polarity causes Rashba polarization to grow in vertical heterostructures. The computed photoresponse and absorption coefficients of the longitudinal heterostructures, which are made up of two distinct components sewn together seamlessly inside the 2D plane[56], indicate optical activity over a broad visible-light spectrum. Simulations of two classes of heterostructures show type-II band alignment, where the VBM and CBM of one part are somewhat greater compared to the other, and consequently good exciton separation.

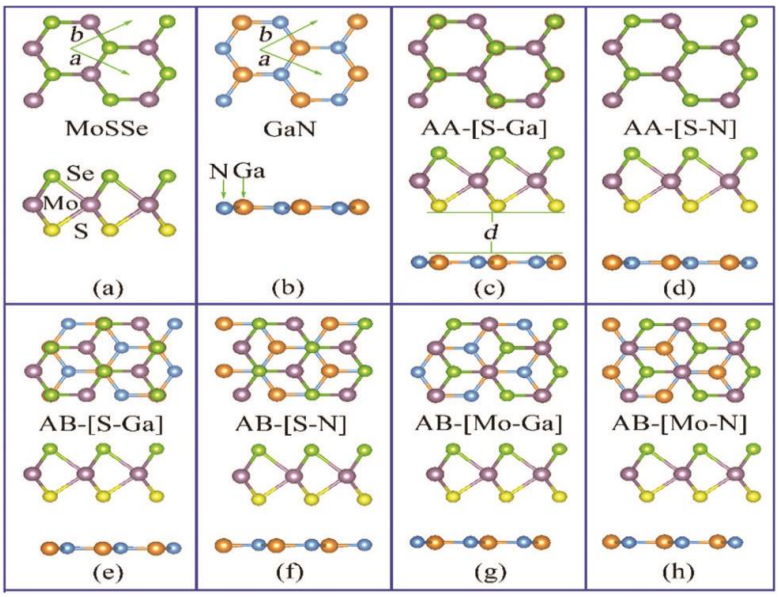


Figure 4: The atomic structure of the MoSSe and their stacking configuration. The primitive cell is colored by green arrows. The Mo, Se, S, N, and Ga atoms are shown as mauve, light green, yellow, blue, and orange spheres, respectively. The interlayer distance between the top and bottom layers is denoted by the ‘‘d’’ letter [57].

Additionally, MoXY/WXY (X, Y = S, Te, and Se) Janus heterostructures generated by several Janus TMD types were studied by Rawat et al.[58]. The researchers found that the band gap of Janus TMDs can be significantly altered across the infrared to ultraviolet spectrum, depending on their composition and structure.

They have also been done on heterostructures composed of Janus TMDs interfaced with other traditional 2D materials. For instance, we looked into the MoSSe/XN (X = Al, Ga) heterostructure produced when mixing Janus MoSSe with nitride semiconductors[48].

Because the Janus MoSSe monolayer's two sides are unlike one another, based on the Se- or S-side of MoSSe faces the monolayer of XN, two distinct vertical heterostructures (SeMoS/XN and SMoSe/XN) can develop. According to the simulations, AB-(S-Ga) stacking yields SeMoS/GaN with the most minimum formation energy, making it the energetically preferred heterostructure. The computed band gaps range from approximately 0.77 eV (SMoS/GaN, AA-(S-Ga)) to approximately 1.63 eV (SMoSe/GaN, AB-(Ga-Mo)), covering the near visible-infrared aera.

The band gap was tweaked to values between 0.77 and 1.47 eV, which are still in the near visible-infrared region, by shifting the location of the S and Se atoms concerning the GaN layer. Recently, Vu et al.[9] used first-principles simulations to examine the heterostructure of WSeTe/graphene. Due to the weak vdW interactions, they discovered the electronic characteristics of graphene and Janus WSeTe are well retained in the heterostructure of WSeTe/graphene.

Compared to isolated graphene and Janus WSeTe monolayers, the optical absorption of the WSeTe/graphene heterostructure is enhanced in the visible and UV light ranges. The visible light absorption coefficient of the graphene/WSeTe heterostructure can reach $5 \times 10^{-4}$ $cm^{-1}$, which is greater than the isolated Janus WSeTe monolayer. First-principles calculations were utilized by Zhao et al.[59] to analyze the electrical characteristics of a Janus MoSSe sheet in contact with a zero-gap germanene electrode. The simulations show that based on whether germanene confronts the Se- or S-side of MoSSe, the structural and electrical features of the two potential interfaces are noticeably dissimilar.

Particularly, simulations of both types of interfaces indicate that the Schottky to Ohmic behavior transition is induced by in-plane tensile strain and that a zero Schottky barrier height can result in the formation of an Ohmic contact when the depth of MoSSe is increased from monolayers toward bilayers.

In addition to adjusting the heterostructure's Schottky barrier, the intrinsic dipole moment also regulates the system's charge carrier mobility and dynamics. Graphene and JTMDsheets combined with vdW sandwich heterojunctions (G/JTMDs/G) for solar cells were explored by Liu et al.[60] using first-principles simulations to examine the electrical structures and dynamics of photo-generated carriers. They discovered that the inherent built-in electric field in JTMDs produces an asymmetric potential that may be used to facilitate the separation and transfer of photogenerated carriers from JTMDs to various graphene layers. Such an improved separation is very directed and occurs in a matter of hundreds of femtoseconds thanks to the integrated electric field in the heterostructure of G/JTMDs/G.

Furthermore, the Se-side with the smaller (higher) potential can transport photogenerated electrons (holes) to the graphene sheets, but the recombination of electrons (holes) is stifled by the considerable distance between their final donor and acceptor states. The simulation results indicate

that, when compared to an isolated graphene sheet, the graphene/WSeTe heterostructure exhibits higher carrier mobility for both electrons and holes. Particularly noteworthy is the finding that the heterostructure can open a band gap of approximately 10 meV near the graphene Dirac cone.

## 2.4. BASIC ELECTRONIC PROPERTIES

Low-dimensional Janus MXY TMDs exhibit unique electronic properties due to the varying sizes and electronegativities of the constituent atoms. This results in different bond lengths and dipoles, which break the mirror symmetry of Janus MXY monolayers. Notably, regardless of the interface structure, all Janus MXY (M = W, Mo; X, Y = S, Te, Se) are semiconductors. Even though the system's stoichiometry determines the band gap of Janus monolayers, atom-specific patterns can be discovered. For instance, PBE measurements indicate that converting S into Te at the Y or X place of MoXY results in a 1.56 eV to 1.02 eV band gap reduction. When compared to PBE results, the band gap rises by around 0.5eV when applying the HSE functional.

As the M-atom in Janus MXY monolayers changes from Mo to W, the system's larger atomic radius leads to a broader band gap. Other metal atoms exhibit this pattern as well. It was observed that the band gap of dynamically, thermally, and mechanically stable Janus MXY monolayers with M = Ti, Zr, and Hf changes from 0.74 to 2.88 eV as the atomic radius of the M-atom increases[45].

Other simulation results demonstrate that, except SnOTe, nearly all Janus SnXY monolayers are stable. Except for Janus materials that include Te, the anticipated band gaps vary within the range of 0.33-1.74 eV for X, and Y compositions, corresponding to the near-visible and infrared regions of light[61].

In addition to composition, the electrical characteristics of MXY are affected by significant shifts in band gap for the 1-T and 1-H phases, as shown in Figure 1. The Janus MoSSe 1-T phase, for example, has been identified as a narrow band gap semiconductor and has even been predicted to exhibit metallic behavior [62]. It has also been demonstrated that the Janus WSeTe monolayer with a 1-H phase is a semiconductor with an indirect band gap of 1.1 eV, in contrast to the 1-T phase, which is semi-metallic.

A little kinetic barrier of approximately 0.66 eV must be surmounted between two phases of WSeTe for the structural phase change from 1-H to 1-T to occur[63]. In contrast to these instances, a close investigation of M2XY (M = Ga, In; X, Y = S, Se, Te) monolayers reveals that each of

these systems is a semiconductor with band gaps in the range of 0.89 eV to 2.03 eV[64,65]. These results demonstrate the strong dependence of the band gap of Janus monolayers on both composition and phase, confirming the promise and prospects for the function-tailored design of this class of materials.

For Janus MoOTe, ΔU can be raised even further to 3.26 eV[41]. The presence of an electrostatic dipole (and the accompanying potential step) perpendicular to the system's plane makes the placement of the valence and conduction band boundaries on the Janus MXY monolayer with different faces stand out in addition to the considerable variations. Studies have shown that such a potential difference can enhance the generation of photoexcited electrons and reduce the band gap of the system to levels below 1.6 eV, enabling efficient infrared water splitting[44].

The focus of this thesis is to optimize the electronic structures of both MoSTe and ZnO monolayers, as well as their 2D van der Waals interactions, to enhance their performance in photovoltaic and photocatalytic water-splitting applications.

## 2.5. POTENTIAL APPLICATIONS

### 2.5.1. PHOTOCATALYTIC WATER SPLITTING

The photocatalyst should have an appropriate band gap, band edge location, and good carrier mobility for successful photocatalytic water splitting. Different Janus materials have been proposed as suitable photocatalysts for water splitting because of their enormous configurable band gaps, and band edge placements for ideal redox potentials[64,66,67]. Using first-principles calculations, Ma et al.[68] investigated the potential of Janus MoSSe monolayers for water-splitting photocatalysis under the application of isotropic and uniaxial strains. For water-splitting reactions, MoSSe monolayer surfaces exhibit stronger H2O molecule adsorption than MoS2 surfaces. Guan et al.'s.[40].First-principles calculations also indicated that Janus MoSSe multilayers might perform very well at splitting visible light. Many Janus 2D materials, including JMoXY (X, Y = S, O, Te, and Se)[34], PtSSe[30], and $XM_2Y$ (X, Y = S, Te, Se; M = In, Ga)[43] monolayers, have all been thoroughly examined in terms of their photocatalytic activity using first-principles simulations. Recently, it was found that Janus heterostructures could be effective water-splitting systems. The structural and electrical properties of Janus MoSSe and nitride XN (X = Al,

Ga) heterostructures were examined using first-principles computations[69,70]. According to the simulations, the MoSSe/AlN heterostructures have indirect band gaps between 1.00 and 1.68 eV. The main mechanism of this unique behavior is the intrinsic electrostatic dipole of the system, which leads to an electrostatic potential difference between its two sides and the distribution of VBM and CBM on opposing sides of the heterostructure.

### 2.5.2. PHOTOVOLTAIC APPLICATIONS

In the Janus TMD monolayer, the built-in vertical EF due to the asymmetry can weaken the exciton binding strength. The strong Coulomb screening and decreased wave function overlap between e and h brought on by the EF will drastically slow down recombination and lengthen the exciton lifetime. By time-domain density functional theory (DFT) calculations, Jin predicted that the exciton lifetime in the Janus-MoSTe monolayer can be up to 1.31ns[66]. To date, some appealing features of Janus TMDs as predicted from theoretical simulations have been verified in experiments. Transient absorption findings indicate that the excitons in these materials are 30% faster than those observed in conventional TMDs. Moreover, the radiative recombination lifetime of excitons is significantly longer than that of pristine counterparts. The results originated from the built-in dipole moment, which can enhance electron-phonon interactions and separate the electron and hole wave functions (Fig.8). These features are helpful for efficiency improvement and charge collection[71].

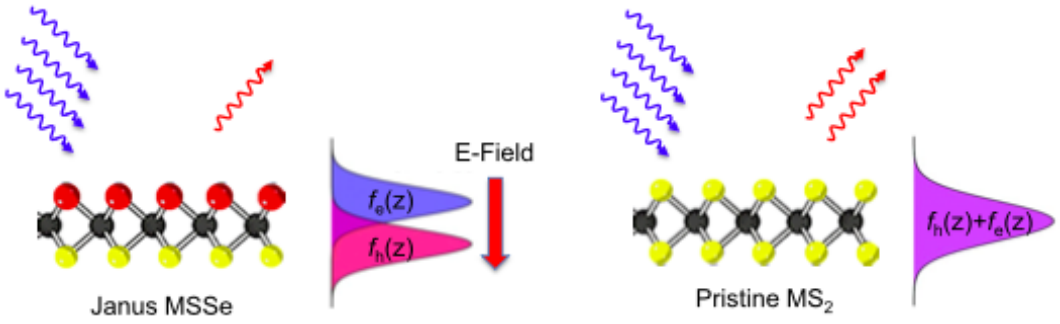


Figure 5: A diagrammatic representation of the wave functions of electrons and holes is depicted for Janus MSSe (M = Mo, W)[71]

# CHAPTER THREE: COMPUTATIONAL METHODOLOGY

The calculations are performed using DFT, which is applied in both the Quantum ESPRESSO [72] and CASTEP packages. First-principles methods can address fundamental questions in material science to design new materials for a huge variety of applications. Predicting new materials for energy conversion, energy storage, and catalysts for the removal of ecologically hazardous exhausts are among the hottest subjects of the day.

In the field of solid-state inorganic materials, density functional theory (DFT) is among the most popular and versatile methods to calculate the energies and structures of different energy storage devices. The calculations involved multiple levels of approximation that accounted for vdW interactions in the heterostructures. These approximation methods included the generalized gradient approximation (GGA), which is well-suited for systems with localized electronic states [73], the hybrid functional (HSE06), and the local density approximation (LDA), which is better suited for systems with a slowly varying electron density.

## 3.1. THE TIME-INDEPENDENT SCHRÖDINGER EQUATION

An overview of the theoretical foundation and computational methods used in the work given in this thesis are provided in this section. The concepts and fundamental ideas of electronic structure computations in general and density functional theory (DFT) in particular will be covered in this chapter. DFT is a method that makes it possible to solve a Schrödinger equation approximatively, precisely, and affordably. Density-functional theory (DFT) associates all the interactions to a uniform variable, the electronic charge density. The hybrid functional HSE06 and van der Waals interactions were considered to calculate the parameters of interest with more accurate results. Finding an answer to the Schrödinger equation is the goal of all calculations using the quantum mechanical and electronic structural methods[74]. The Schrödinger equation plays a crucial role in these methods, as it enables the calculation of all physical properties of the system by providing information about the wave function ($\psi$). This wave function contains all the relevant information related to the positions and spins of the constituent particles within the system. The Schrödinger equation's many-body Hamiltonian accurately describes the microscopic properties of electrons in the fields of chemistry, biology, and material science. While this Hamiltonian contains all the information about a system, not all the information is equally important in practice. Often, the most critical information is found within the system's most stable state. This most stable state is

characterized by the ground state of the many-body Hamiltonian,*i.e.*, the smallest eigenvalue and eigenvector of the many-body Hamiltonian. The Schrödinger equation in its time-independent form can be expressed as:

$$H\psi = E_{Totl}\psi \quad (3.1)$$

The following list of mathematical operations can be used to explain the entire Hamiltonian operator (H), which when applied to the wave function (ψ), will define a system-related property:

$$H = T + T_n + V_{\text{int}} + V_{\text{nn}} + V_{ext} \quad (3.2)$$

where: T=kinetic energy of the electrons,

$T_n$= kinetic energy of the nuclei,

$V_{int}$=potential energy of the interelectron (electron-electron) repulsions,

$V_{nn}$=potential energy of the nuclear-nuclear repulsions and

$V_{ext}$=potential energy of the electron-nuclear attraction (external potential)

$$H = -\frac{\eta^2}{2m_e}\sum \nabla_i^2 - \sum_I \frac{\eta^2}{2M_I}\nabla_I^2 + \frac{1}{2}\sum_{i\neq j}\frac{e^2}{|r_i - r_j|} + \frac{1}{2}\sum_{I\neq J}\frac{Z_I Z_J . e^2}{|R_I - R_J|} - \sum_{i,I}\frac{Z_I . e}{|r_i - R_I|} \quad (3.3)$$

The Born-Oppenheimer approximation is the initial step in simplifying the complexity of the quantum many-body problem, wherein the complexity arising from the electrons and nuclei is separated. As the mass of electrons is over a thousand times smaller than the nuclei of even the lightest element in the periodic table (hydrogen), the Born-Oppenheimer approximation acknowledges that electrons move much faster than nuclei. Consequently, the state of electrons is "enslaved" to the motion of nuclei.

Electrons have a mass that is over 1000 times smaller than that of nuclei[75]. The ground state of the many-body Hamiltonian of the electrons (H_elec), more particularly, gives the following description of the state of the electrons for fixed nuclei positions:

$$H_{ele} = -\frac{\hbar^2}{2m_e}\sum_i \nabla_i^2 + \frac{1}{2}\sum_{i\neq j}\frac{e^2}{|r_i - r_j|} + \sum_i V_{ext}(r_i) \quad (3.4)$$

The Schrödinger equation can now be solved for many body systems with a manageable level of complexity.

## 3.2. DENSITY FUNCTIONAL THEORY CALCULATIONS

The electronic structure of matter can be efficiently computed using DFT, a variational methodology that relies on electronic density to regulate the system's energy in its ground state.

Currently, DFT is considered the most effective approach for this purpose. The Hohenberg-Kohn theorems[76] and the contributions of Kohn and Sham[77] were pivotal in the initial advancements of contemporary DFT.

### 3.2.1. HOHENBERG-KOHN THEOREMS

The quantum many-body problem is reduced to the electronic structure problem via the Born-Oppenheimer approximation. Further approximations are required since the electronic structure problem still exhibits exponential complexity with respect to the number of electrons N. Less consensus has been reached on the Born-Oppenheimer approximation than on the approximation of the electronic structure problem. Different electronic structure hypotheses with varying degrees of accuracy and efficacy have been put forth. After decades of research, density functional theory is now the most popular electronic structure theory because it frequently achieves the optimum balance between accuracy and efficiency.

At the core of density functional theory lies the Hohenberg-Kohn theorems, which provide a fundamental framework for addressing complex many-body problems through the use of an essential quantity, the electronic density, rather than the wave function[76,78]. The Born-Oppenheimer equation is not easy to solve simplified Schrodinger equation, since the electrons and nuclei that compose materials comprise a strongly interacting many-body system that cannot yet be solved directly. Density functional theory provides an approximate solution for finding the ground state of a many-body system.

The Hohenberg-Kohn Theorems define the energy functional as follows:

$$E[\rho(r)] = \int V_{ext}(r)\rho(r)d\big(\rho(r)\big) + F[\rho(r)] \quad (3.5)$$

### 3.2.2. KOHN-SHAM EQUATIONS

The ground-breaking work is provided by Kohn and Sham [77]. In 1965, Kohn and Sham presented an approach that involved substituting the challenging interacting many-body system with an independent particle problem, while still incorporating the many-body effects, such as the exchange-correlation function. Kohn and Sham's theorem assumes that the ground state density of the original interacting system is equal to that of an equivalent noninteracting electron system with the same external potential. To solve the Kohn-Sham equations, a set of hypothetical non-interacting electrons is initially utilized. These electrons are employed in a manner that ensures their density matches the exact density of the real system. The Kohn-Sham equations are

formulated with respect to a local effective external potential, typically denoted as $(r)$, which governs the motion of the hypothetical electron.

$V_{KS}(r) = \int E_{ke}\,[\rho(r)] + \nu_{ext}(r) + \nu_{xc}(r)$(3.6)

The first term represents the Hartree potential, [$(r)$], the second is the Coulombic interaction between the electron and nuclei, and the final term, $(r)$, explains the exchange-correlation functional. A hypothetical set of noninteracting electrons serves as the starting point for solving the Kohn-Sham equations. They are used, however, in a way that ensures the density of these hypothetical, non-interacting electrons is the same as the density of the actual system. The local effective external potential, typically represented as (r), in which the imaginary electron moves is used to describe the Kohn-Sham equations.

Equation 3.6 should be understood to refer to the energy of a group of non-interacting electrons, as described by the E_ke [ρ(r)] term. Moreover, it is worth noting that the Hartree term (equation 3.7) does not take into account the correlation between electron motions. Instead, the interacting electrons are characterized by the summation of classical pairwise interactions that stem from their charge densities.

$E_H[\rho(r)] = \frac{1}{2}\iint \frac{\rho(r_1)\rho\rho(r_2)}{|r_1 - r_2|}\,dr_1 dr_2$ (3.7)

To obtain a fixed solution for the Schrödinger equation, equations 3.6 and 3.7 must be combined and then minimized to ρ(r). This procedure yields the Kohn-Sham equation, which takes on a form similar to that of the Schrödinger equation, as demonstrated below:

$\left[-\frac{\hbar^2}{2m_e}\nabla^2 + V_{eff}(r)\right]\Psi_i(r) = E_i\Psi_i(r)$(3.8)

The Kohn-Sham orbitals containing the hypothetical non-interacting electrons are represented by $\Psi_i(r)$, while the corresponding orbital energies are denoted by $E_i$. Additionally, the effective potential of the system is represented by the $(V_{eff})$term.This final effective potential term $(V_{eff})$ can be further separated according to equation 3.9:

$V_{eff}(r) = V_{ext}(r) + \int \frac{\rho(r')}{|\boldsymbol{r}-\boldsymbol{r}'|}\boldsymbol{dr}' + \boldsymbol{V_{xc}(r)}$(3.9)

Equation 3.10 relates the exchange-correlation energy functional $(\boldsymbol{E_{xc}[\rho(r)]})$to the exchange-correlation potential $\boldsymbol{V_{xc}(r)}$.The latter term is a component of the Kohn-Sham equation and is responsible for accounting for exchange-correlation effects in the system.

$$\boldsymbol{V_{xc}(r) = \left(\frac{\delta E_{xc}[\rho(r)]}{\delta \rho(r)}\right)} \qquad (3.10)$$

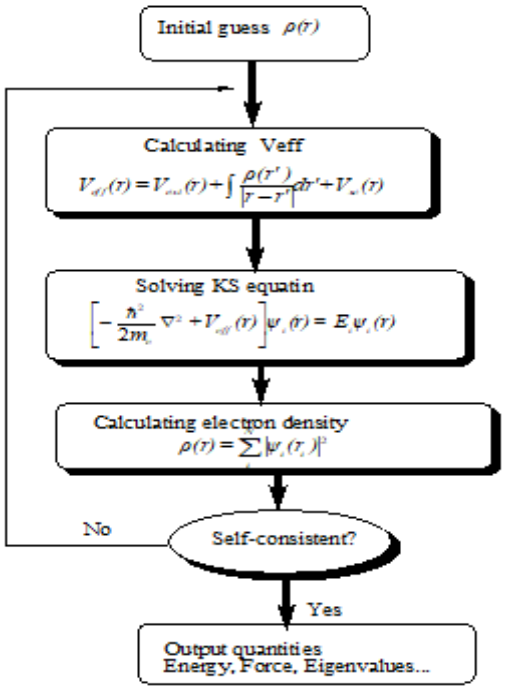


Figure 6: A flowchart that simplifies the self-consistency loop for solving Kohn-Sham equations.

DFT utilizes a combination of the Hohenberg-Kohn theorems and the Kohn-Sham equation to solve the Schrödinger equation for a given system. The iterative process of finding a solution begins with an initial approximation of the electron density (ρ(r)), which is used in equation 3.9 to generate an effective potential (V_eff). This effective potential is then inputted into equation 3.8 to produce a set of Kohn-Sham orbitals for the system. With these orbitals, a refined estimate of the electron density (ρ(r)) can be calculated using equation 3.11.

$$\boldsymbol{\rho(r) = \sum_i^N |\Psi_i(r_i)|^2} \qquad (3.11)$$

The self-consistent field method outlined above generates a converged electron density, which corresponds to the ground-state electron density for the system, as stipulated by the second Hohenberg-Kohn theorem [76].

### 3.2.3. EXCHANGE-CORRELATION FUNCTIONAL

If the exchange-correlation functional (Exc[ρ(r)]) in the Kohn-Sham expression is exact, then the resulting ground-state energy and density will also be exact. However, in reality, it is challenging

to derive an exact exchange-correlation function since the system is often too complex. There are approximations for this term. In contrast to the direct Coulomb contact, which is only electrostatic repulsion, the electron-electron interactions that result from the overlap of electron wave functions are referred to as exchange and correlation. The exchange interaction is primarily concerned with the overlap of electron wave functions with parallel spin. It naturally includes the Pauli exclusion Principle, which does not allow electrons with parallel spins to occupy the same orbital due to the antisymmetric nature of fermion wave functions. Correlation deals with the interaction of electrons with anti-parallel spin. The exchange and correlation effects have a net energy-reducing impact on the system as they counteract the repulsive interactions that would otherwise necessitate the direct Coulomb interaction to maintain the electrons' separation.

Correlation, in particular, has classically proven to be difficult to calculate, due to the incredible amount of computing power required for an exact value of the correlation energy to be obtained. However, the Kohn-Sham equations have the exchange and correlation potentials as functional of the local density only. This makes the calculation of these energies tractable. The accuracy of the whole DFT technique relies upon finding a good approximation of this quantity. At present, the majority of functional approximations for the exchange-correlation functional (Exc[ρ(r)]) are derived from either the LDA or GGA, which can be viewed as an extension of the LDA.

### 1. LOCAL DENSITY APPROXIMATION (LDA)

Various schemes have been developed to derive approximate forms of the exchange-correlation energy function. The main source of error in DFT usually occurs from the approximate nature of $E_{xc}$.[78]. Using the LDA the exchange-correlation function is represented as follows:

$$\boldsymbol{E_{xc}^{LDA}[\rho] = \int \varepsilon_{xc}^{hom}(\rho)\rho(r)drr} \quad (3.12)$$

For a variety of materials, it is typically discovered that using LDA, the replication of features such as bond lengths, crystal structure, and phonon frequencies is highly accurate. In the LDA approach, it is assumed that the exchange-correlation energy density is equal to the energy density of a homogeneous electron gas with the same density. The accuracy of this approximation depends on how well the electron density in the crystal can be approximated by an electron gas. While this concept provides a reasonable approximation for metals, it fails to work well for highly inhomogeneous compounds.

The Kohn-Sham equations can be calculated, although they are sometimes erroneous due to the approximation that the Kohn-Sham exchange-correlation functional depends only on the local density. When attempting to determine the electronic structure of metals and insulators, in particular, the Kohn-Sham equations encounter difficulties, albeit for quite different causes. The exchange-correlation function solely depends on the local density, which causes difficulty with metals. The Fermi surface won't be accurate, even though the local density will be replicated and the Kohn-Sham equations will accurately predict the crystal's metallic nature.

### 2. GENERALIZED GRADIENT APPROXIMATION (GGA)

For a wide range of systems, LDA performs well in terms of atomic structure, elastic characteristics, and vibrational properties. However, LDA is not accurate enough to describe the energies of chemical reactions, leading to an overestimate of the binding energies of molecules and solids in particular. For real systems, there are always some variations in the electron density to the position. The variation of the electron density with position is attempted to include in various approximations for the exchange-correlation energy functional (Exc[r)] term). The GGA has been developed to address some of these deficiencies[79], and the XC function is represented as follows.

$$\boldsymbol{E_{xc}^{GGA}} = \int \boldsymbol{\epsilon_{xc}}(\boldsymbol{\rho_{\uparrow}}, \boldsymbol{\rho_{\downarrow}}, \boldsymbol{\nabla\rho_{\uparrow}}, \boldsymbol{\nabla\rho_{\downarrow}})\boldsymbol{\rho}(\boldsymbol{r})\boldsymbol{d^3r} \quad (3.13)$$

Utilizing GGA-based calculations leads to greater accuracy in the determination of lattice, band gaps, and structural optimizations compared to equivalent LDA calculations. The GGA accounts for the exaggerated binding energies seen in the LDA. The most common GGA parametrization is the PW91[80], PBE [81], and RPBE [82]. PW-91 used to be almost the standard function in physical science but has been replaced by PBE in recent years. The research presented in this thesis was conducted using the Quantum ESPRESSO software.

### 3. VAN DER WAALS FUNCTIONALS

Since the London dispersion forces are excluded in the semilocal and hybrid functionals, it is impossible to apply them with accuracy to systems in which they are crucial. The semilocal or hybrid functional can have a correlation dispersion term added to it to better account for the London dispersion forces in DFT. The resulting van der Waals functionals are as follows:

$$\boldsymbol{E_{xc}} = \boldsymbol{E_{xc}^{SL/hybrid}} + \boldsymbol{E_{c,disp}} \quad (3.16)$$

where the terms $E_{c,disp}$ that have been proposed in the literature dispersion[83].

## 4. HYBRID FUNCTIONALS

In comparison to semilocal approaches, such as GGA, hybrid functionals, which combine the Hartree-Fock (HF) and Kohn-Sham theories[84], can be more accurate, especially for nonmetallic systems. They are suitable for band-gap computations, for instance. The exchange part of hybrid functionals is made up of a linear combination of HF and semilocal (such as GGA) exchange:

$$E_{xc}^{hybrid} = \alpha E_x^{HF}(1-\alpha)E_x^{GGA} + E_c^{GGA} \qquad (3.17)$$

Hybrid functionals can be classified into different families based on the interelectronic range at which the HF exchange is applied. In practical terms, for periodic solids, short-range hybrid functionals like HSE are preferred since they promote faster convergence concerning the number of k-points. It is worth noting that hybrid functionals are computationally more demanding compared to semi-local methods. A comprehensive study of the HSE03/HSE06 functional performance compared to the PBE and PBE0 functionals[85]. The B3LYP functional is applied to solid-state systems[86].

# CHAPTER FOUR: RESULTS AND DISCUSSIONS

## 4.1. COMPUTATIONAL DETAILS

First-principles calculations were carried out on the monolayer of ZnO, MoSeTe, and Janus ZnO-MoSeTe heterostructures using DFT with a plane-wave basis along with Projector Augmented Wave (PAW) pseudopotentials (PP)[87]. These calculations were performed through the implementation of Quantum-ESPRESSO and CASTEP codes [88,89]. The geometry optimization calculations were performed using the GGA-PBE method, which incorporates a van der Waals correction through the gramme-D2 method[87]. All DFT calculations of the monolayers (ZnO& MoSeTe) and heterostructure of ZnO/MoSeTe have been performed using PBE ultrasoft pseudopotentials for core interaction under the framework of Quantum-ESPRESSO. In this work, first, we decide the appropriate values of the K-point, cutoff energy(Wfc), charge density(ecutrho), and lattice parameter. Self-consistent calculations (convergence test) were performed by adjusting the system card parameters to obtain a converged minimum total energy. For geometric optimization, the 'relax' calculation is performed to optimize the atomic position of the monolayer and heterostructure. For Brillouin zone sampling, an optimized k-point was applied using the Monkhorst–Pack scheme with the 9x9x1 grid for the convergence test of ZnO and Janus MoSeTe monolayers, and the heterostructures. To describe the interaction between core and valence electrons, a plane wave with a kinetic cutoff energy of 70Ry and Ecutrho of 840Ry was utilized. The geometric Structures are relaxed until forces are below 1 meV$Å^{-1}$.The PBE functional with the vdW correction (DFT-D2) was used to treat the interfacial interactions between ZnO and MoSeTe heterostructures

## 4.2. CONVERGENCE TEST

Convergence testing is a technique for improving simulations to use limited computational resources efficiently and produce useful findings. In this study, we performed various SCF calculations for the k-points grid, kinetic energy cutoff, charge density cutoff, and lattice parameter optimization to determine the fundamental parameters to obtain the optimum energy.

### 4.2.1. THE K-POINT OPTIMIZATION

Early computational studies focused on an affordable selection of k-points for Brillouin zone sampling to allow computations for real-space unit cells with a lot of atoms to be performed[90].

However, for correct computations, a better set of special k-points should be used. More grid points can be taken to obtain more accurate results, but doing so is expensive in terms of calculation.

SCF calculations were conducted on the total energy using various k-point grids, ranging from 1×1×1 to 16×16×1. The total energy varies depending on the change in k-points and converges, as indicated in Figure 7(a and b). The total energy and k mesh values converged linearly starting from 5x5x1, and we can begin with those values to choose the proper basis set size. By taking into account the limitations of computing resources, the optimal set of k-point values selected for ZnO and MoSeTe monolayers are 9x9x1, with a significantly small total energy change.

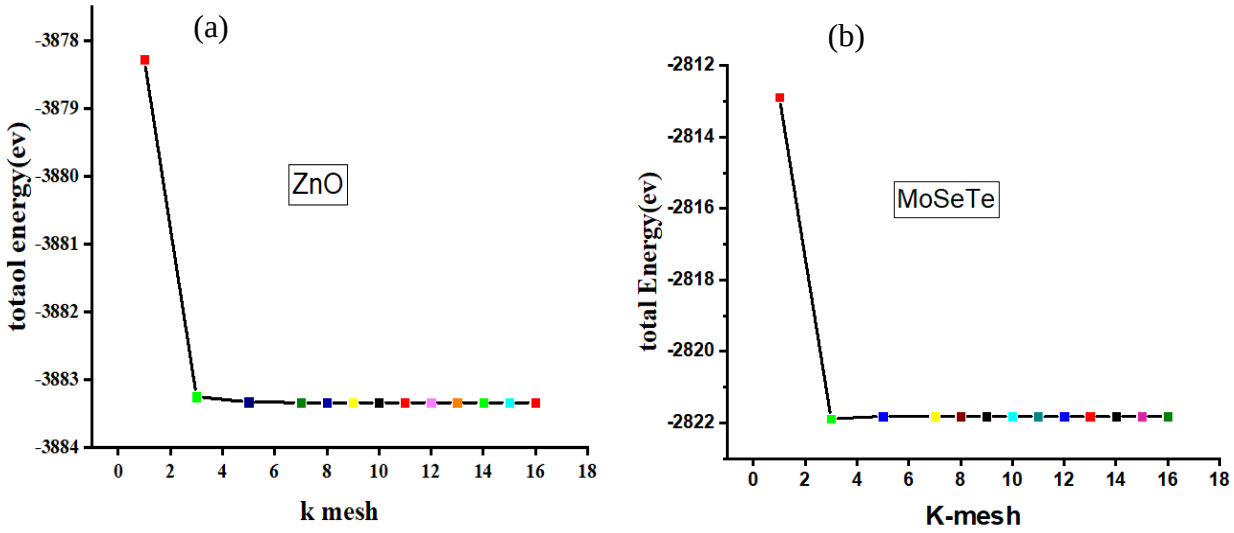


Figure 7: Energy vs K-mesh of (a) ZnO and (b) MoSeTemonolayers computed using PBE

### 4.2.2. BASIS SET SIZE

If the scripting is general in the Quantum ESPRESSO module, the two key flags Ecut (wfc) and Ecut (rho), which refer to cutoff energy, can be located in the & SYSTEMcard name list. Wave function kinetic energy cutoffs are indicated by Ecut (Wfc), while charge density cutoffs are indicated by Ecut (rho). The DFT can be calculated using the number of plane waves specified by Ecut. The calculation accuracy increases but the calculation time increases when the value for the computation of plane waves is put to a large number. Achieving the appropriate balance between the maximum kinetic energy cutoff and the number of plane waves requires adjusting the number of plane waves. During calculation keeping Ecut(rho) as a multiple factors of Ecut(wfc) is

essential. Then we can vary it first, maintaining Ecut(rho) at identical factor time's Ecut (wfc). The scenario can also be repeated for Ecutrho after the appropriate value for Ecut (wfc) has been obtained.

From Figure 8 (a and b) we understand the convergence is achieved at higher Ecut(Wfc) and higher total energy. For both ZnO and MoSeTe monolayers, the good set values of Ecut (Wfc) are 70 Ry, which was selected with a small change in total energy.

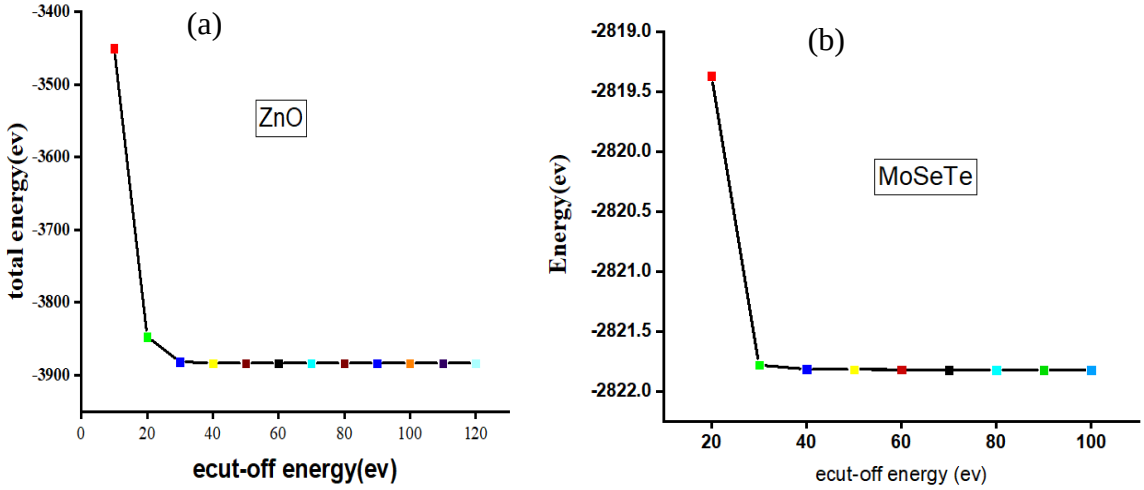


Figure 8: Total energy vs Ecut(Wfc) of (a) ZnO and (b) MoSeTeMonolayer's computed usingPBE

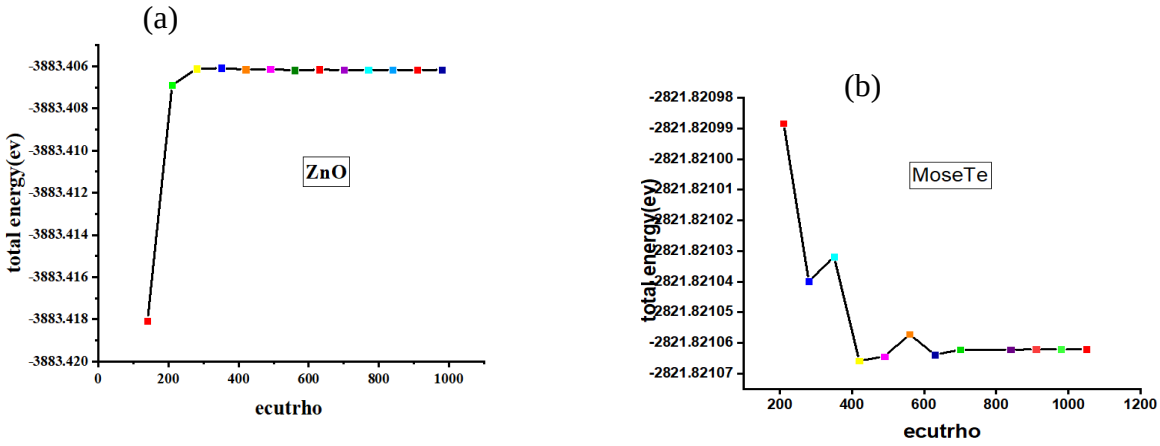


Figure 9: Total energy vs Ecut(rho) of (a) ZnO and (b) MoSeTemonolayers computed usingPBE

Figure.9 shows that the total energy convergence of ZnO is achieved linearly starting from 350 Ry Ecutrho, whereas MoSeTe starts from 630 Ry. To obtain the best structure, the appropriate values

of Ecut (rho) for both ZnO and MoSeTe monolayers should be set to 840 Ry, which is best for the next calculation.

### 4.3. LATTICE CONSTANT OPTIMIZATION

After the crystal lattice constant of monolayers is optimized, 2D ZnO/MoSeTe heterostructures must be constructed. Therefore, Janus MoSeTe and ZnO monolayers are very important to design vdW heterostructures. By providing a starting lattice constant that was less than the anticipated value when calculating its total energy, ZnO and MoSeTe lattice constant optimization was carried out. We repeated the calculations, and at the end of each stage, we had new lattice constants and new total energy. The iteration continued until we obtained the smallest total energy. After gating the minimum total energy and optimized lattice constant, the crystal structure must be relaxed to achieve a stable atomic position for the next calculation. The optimized/calculated lattice parameters of ZnO and MoSeTe monolayers in the ranges of 3.20 Å to 3.40Å and 3.34Å to 3.46 Å are exhibited in Figure 10(a and b) respectively. The equilibrium lattice constant of ZnO is 3.27 Å and that of MoSeTe is 3.40Å. Therefore, this value gives the minimum total energy of monolayers. In Table 1 the optimized lattice parameters of ZnO and MoSeTe are compared with those of earlier studies and closely matched with those previous works.

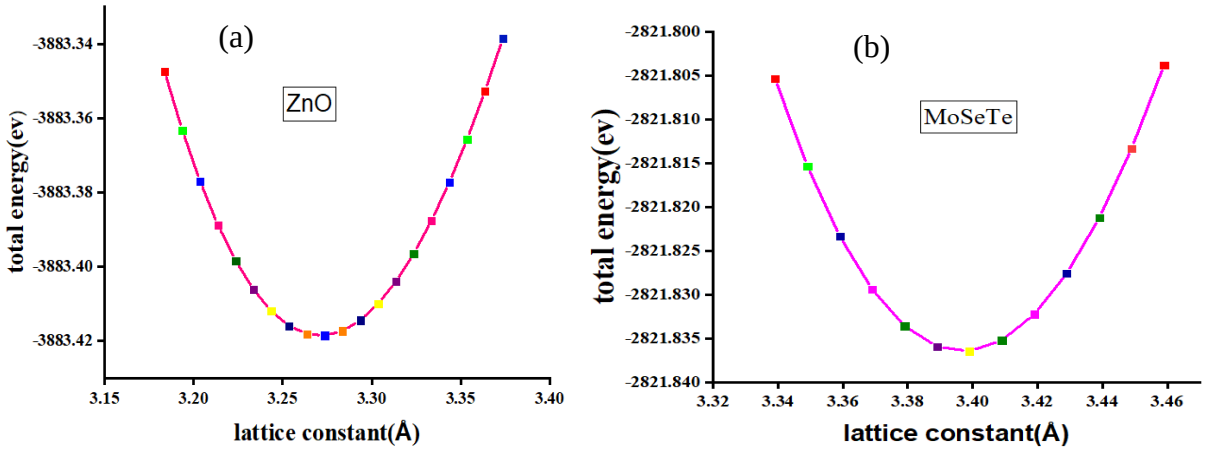


Figure 10: Total energy vs lattice parameter of the(a) ZnO and (b) MoSeTe monolayers computed using PBE.

## 4.4. STRUCTURAL OPTIMIZATION OF ZnO AND JANUS MoSeTe MONOLAYERS

The most stable heterostructures employing 2D semiconductors require lattice mismatch. Heterostructures are essential for the formation of vdWHs because of their well-suited structural character. Multilayer vdWH, in which individual covalently linked layers are held together by weekly vdWH forces without dangling bonds, is a promising method of merging several 2D materials to attain desirable features for many TMDs.

The lattice mismatch calculation was performed using the formula:

$$\text{Lattice mismatch}(\%) = \frac{\left(\text{JTMDs(lattice parameter a}(\text{Å})\right) - \text{ZnO( lattice parameter a}(\text{Å})\right) \text{x}100\%}{JTMDs\left(\text{lattice parameter a}(\text{Å})\right)}$$

Table 1. Lattice Parameters and Lattice Mismatches of Monolayers Calculated Using PBE.

| MXY | Calculated lattice constant a(Å ) | References lattice constant a(Å ) | Calculated mismatch values (%) |
|---|---|---|---|
| ZnO | 3.27 | 3.29[87],3.29[91] ,3.24[92] | |
| MoSeTe | 3.40 | 3.42[89], 3.41[93] | 3.72% |

Table 1 shows that the lattice mismatch of the optimized lattice parameters of the two monolayers is below 5%, and the ZnO and MoSeTe layers are completely coherent. The MoSeTe/ZnO lattice mismatch is quite small(3.72%), which is suitable to design heterostructures in terms of the vdW interactions and shows a possibility of fabricating the structures experimentally. The weak vdW interaction will play a major role because MoSeTe and ZnO do not have any significant interactions between them. Based on first-principles calculations, new 2D heterostructures were designed using monolayers of MoSeTe and ZnO.

## 4.5. ELECTRONIC PROPERTIES OF ZnO AND MoSeTe MONOLAYERS

For potential electronic and optoelectronic applications, the band gap of 2D materials is a crucial factor. The electronic band structure and partial density of states of MoSeTe and ZnO monolayer structures investigated using GGA-PBE are depicted in Figs. 14(a and b) and 15 (a and b). Janus MoSeTe monolayer and ZnO Monolayer are semiconductor materials with indirect band gap and direct band gap of 1.49 eV and 1.68 eV respectively. Their band gap was also calculated using

HSE ( ZnO = 2.99 eV & MoSeTe = 1.86 eV) and compared with previous work research. Figure 14 shows that the CBM and VBM of the ZnO monolayer are positioned between the Γ-K and M- Γ paths, and for monolayer MoSeTe the VBM is located at the K path, and the CBM is between the Γ-K path. The calculated band gap results closely agree with the earlier work reported values computed using GGA-PBE[89,93,94].

Table 2 The calculated lattice constant (Å), calculated band gap (eV), work function ( ϕ in eV), and valence and conduction band edge with respect to vacuum (EVB & ECB) for the monolayer.

| monolayer | ZnO | MoSeTe |
|---|---|---|
| a | 3.27 | 3.40 |
| Eg-PBE | 1.676(dir) | 1.487(indir) |
| Eg_HSE | 2.986 | 1.856 |
| ϕ | 5.064 | 5.073 |
| EVB | -5.062 | -5.07 |
| ECB | -3.385 | -3.583 |

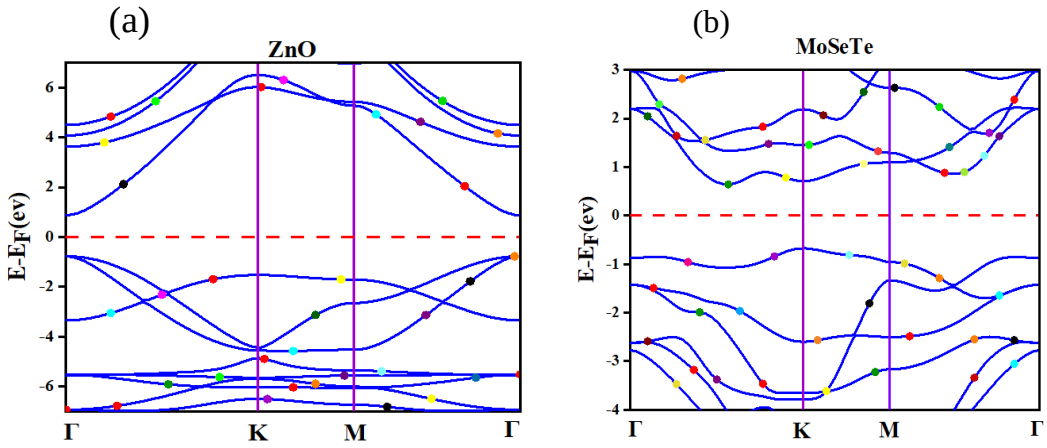


Figure 11: The electronic band structure of ZnO and MoSeTe monolayers

The PDOS of ZnO and MoSeTe monolayers were computed using GGA-PBE as exhibited in Figure 12 (a&b). Mo-4d atoms dominate in the states of MoSeTe close to the Fermi level of the CBM and VBM, whereas O-2p atoms have a significant impact on the VBM of ZnO. The CB (located between -7.0 eV and -0.5 eV) of MoSeTe is mainly composed of Mo-4d and Se-2p states and is dominated by Mo-4d states. In the conduction band for MoSeTe, the Mo-4d plays the main

role from 0.5 eV to 3.8 eV. Furthermore, O-2p atoms predominate in the states of ZnO, which are far from the Fermi level of the CBM.

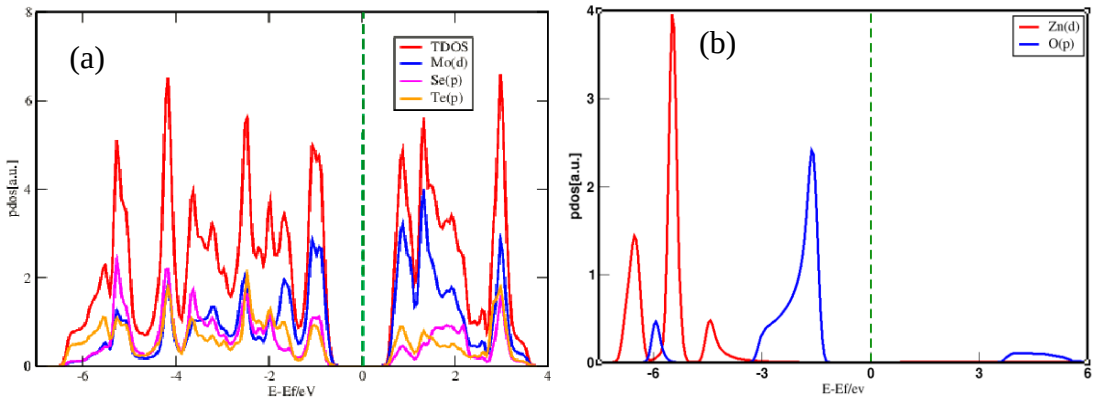


Figure 12: The PDOS of (a) ZnO and (b) MoSeTe Monolayers computed using PBE

## 4.6. OPTIMIZED HETEROSTRUCTURES OF ZnO/MoSeTe

To identify the best Heterostructures, we prepared eight stacking pattern structures by translating, inverting, and rotating one monolayer concerning the other, and their structures were initially optimized.

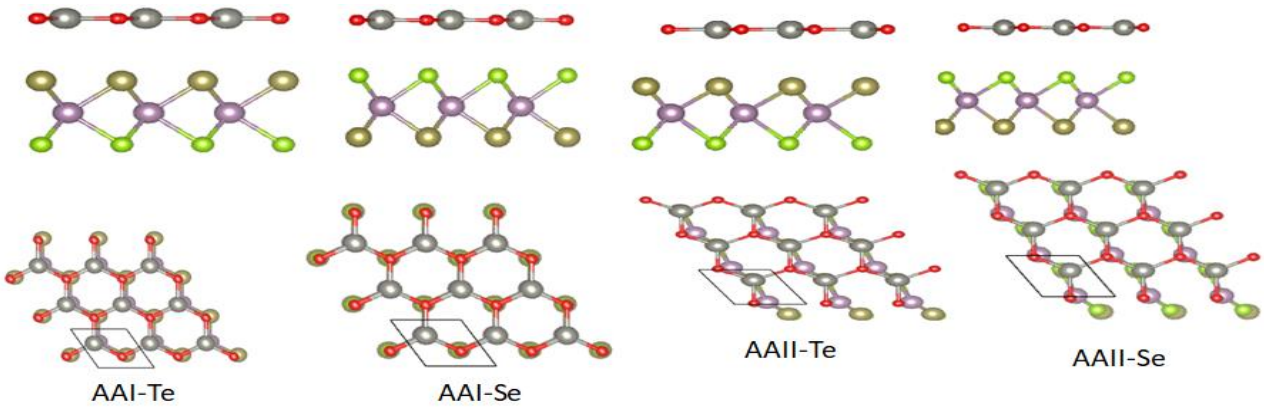

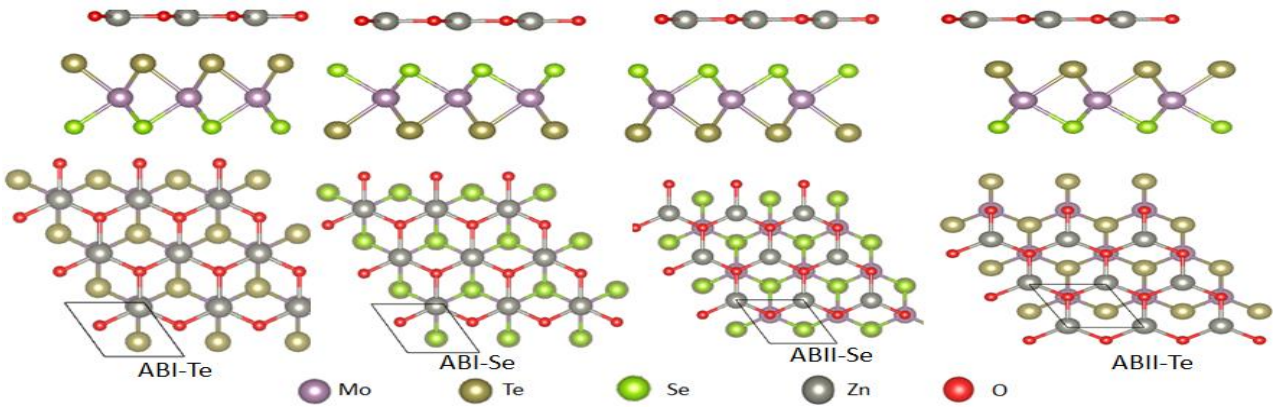


Figure 13: Stacking configuration of the ZnO/MoSeTe heterostructure.

The symbols AA and AB show the stacking configuration, whether the two hexagonal lattices are justified on top of one another or shifted. I and II represent whether the Zn is aligned below the Mo metal or the Se/Te atom of Janus MoSeTe. Te and Se indicate that the Te and Se halogen atoms face the ZnO monolayer.

The binding energy ($E_b$) determines the stability of the heterostructures[95–97]. Therefore, the $E_b$ of all symmetry stacking orientations of ZnO with MoSeTe is computed to decide the lowest energy structures.

The binding energies of the different stacking configurations of ZnO–MoSeTe heterostructures are calculated using

$$E_b = E_{ZnO/MoSeTe} - (E_{ZnO} + E_{MoSeTe}) \quad (4.1)$$

where $E_b$ is the binding energy, $E_{ZnO/MoSeTe}$ is the heterostructures' total energy, and $E_{ZnO}$ and $E_{MoSeTe}$ are the total energies of the ZnO, and MoSeTe monolayers, respectively.

Table 3. Lattice Parameters, Interlayer Distances, and Binding Energies of ZnO/MoSeTe Heterostructures were computed.

| Stacking Patterns | Lattice Parameter a = b (Å) | Interlayer Distance (Å) | Binding Energy (ev) |
|---|---|---|---|
| AAI_Se | 3.33 | 3.09 | -2.55 |
| AAI_Te | 3.33 | 3.39 | -2.55 |
| AAII_Se | 3.33 | 3.05 | -2.26 |
| AAII_Te | 3.33 | 3.28 | -2.48 |
| ABII_Se | 3.33 | 3.55 | -2.57 |
| ABII_Te | 3.33 | 3.64 | -2.97 |
| ABI_Se | 3.33 | 3.49 | -2.65 |
| ABI_Te | 3.33 | 3.67 | -2.81 |

Of the eight stacking patterns three have the lowest negative binding energy and the more stable stacking modes of ZnO/MoSeTe heterostructures were selected for further study of their electronic properties as shown in Figure 14. We also investigated eight basic stacking patterns of the designed ZnO/MoSeTe hetero-bilayer. The ABII-Te stacking mode was a more stable stacking type depending on the $E_b$ and the interlayer distance, as indicated in Table 3.

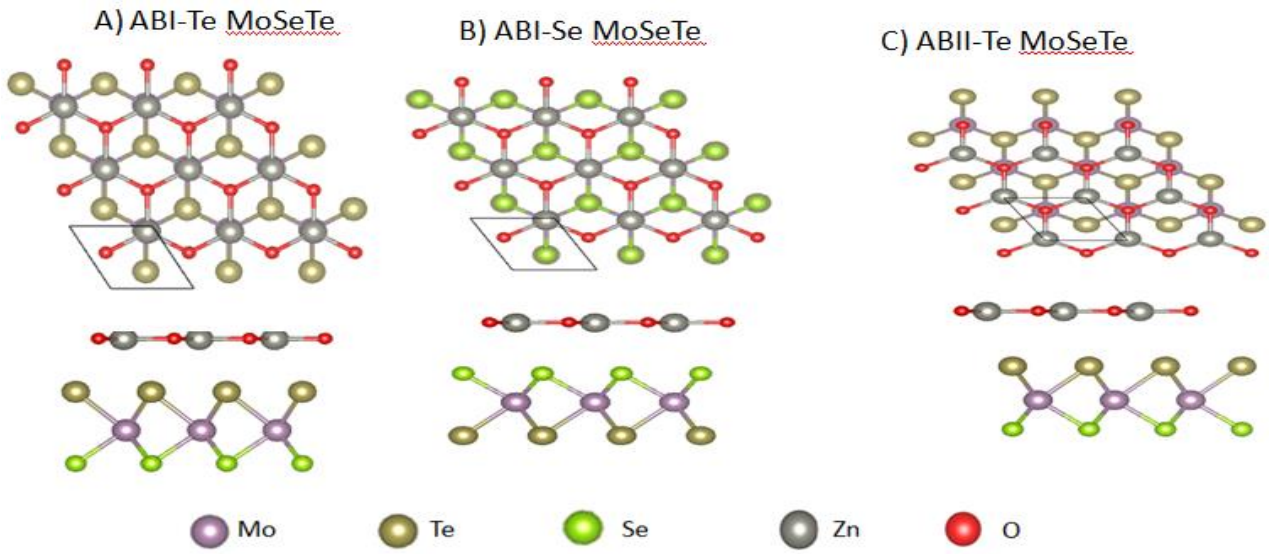


Figure 14: Stacking patterns of the three most Stable ZnO/MoSeTe heterostructures with different stacking orientations.

## 4.7. ELECTRONIC PROPERTIES OF ZnO/MoSeTe HETEROSTRUCTURES

The electric properties of ZnO/MoSeTe heterostructures are expected to be significantly influenced by the various stacking orders and interlayer interactions.

Figure 15 shows the band structures of the different configuration patterns of ZnO/MoSeTe vdW heterostructures, ABI-SeMoSeTe, ABI_Te MoSeTe, and ABII-Te MoSeTe, which are indirect band gaps semiconductors with 1.39 eV, 1.32 eV, and 1.39 eV at the PBE level respectively. As shown in Table 4, all three different stacking of ZnO/MoSeTe materials are semiconductors with band gaps of 1.35eV, 1.33 eV, and 1.36 eV at the HSE level. The VBM of three stacking patterns of ZnO/MoSeTe heterostructures is found at the K path in BZ, whereas the CBM location is shifted to the left side from the K path. Table 4 shows a summary of the results obtained from the ZnO/MoSeTe heterostructure.

Table 4. Optimized lattice constant a (Å), calculated band gap(PBE and HSE in eV), work function ( in eV), and valence, and conduction band edges with respect to vacuum (EVB and ECB) for the heterostructure.

| Heterostructure | ABI_Se MoSeTe | ABI_Te MoSeTe | ABII_Te MoSeTe |
|---|---|---|---|
| a | 3.3269 | 3.3269 | 3.3269 |
| Eg-PBE | 1.385(indir) | 1.318(indir) | 1.39(indir) |
| Eg_HSE | 1.349 | 1.327 | 1.355 |
| ϕ | 4.982 | 5.061 | 5.049 |
| EVB | -4.99 | -4.99 | -5 |
| ECB | -3.605 | -3.672 | -3.61 |

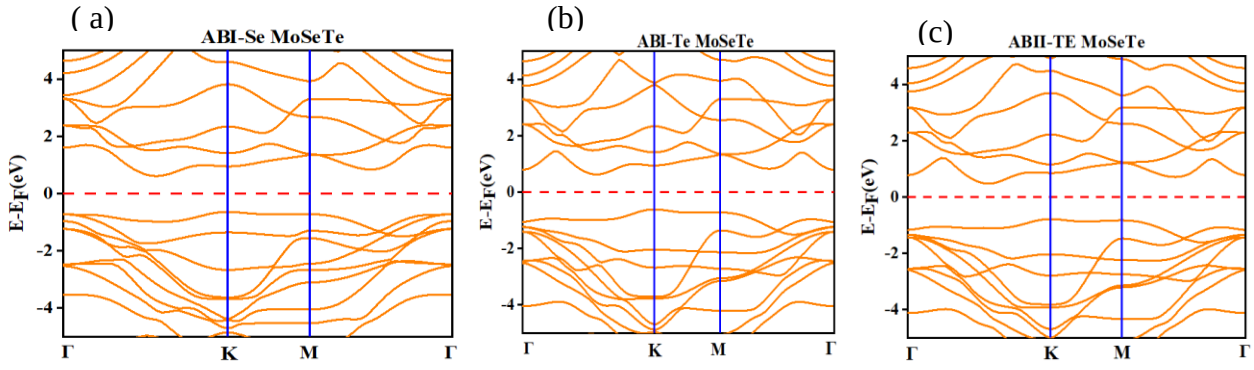


Figure 15: The electronic structure of ZnO/MoSeTe heterostructure

The states close to the fermi level in the ZnO/MoSeTe heterostructures are primarily produced by Mo-d, S-p, Te-p, and O-p orbitals, which originate from the corresponding Mo, Se, Te, and O atoms. The CBM and VBM close to the Fermi level are highly contributed by the Mo-4d orbital. The upper VB (located between –7.0 eV and~ -1 eV) of the ZnO/MoSeTe heterostructure is highly composed of Zn-3d and O-2p orbitals and it is highly contributed by Zn-3d states. On the other hand, the lower conduction band (located between 1 eV and ~ 4 eV) of the ZnO/MoSeTe heterostructure is primarily composed of Mo-4d and Te-2p states and it is highly contributed by Mo-4d states. In addition, the CB of the Mo-4d state acts the main role in determining the electronic characteristics of the heterostructures.

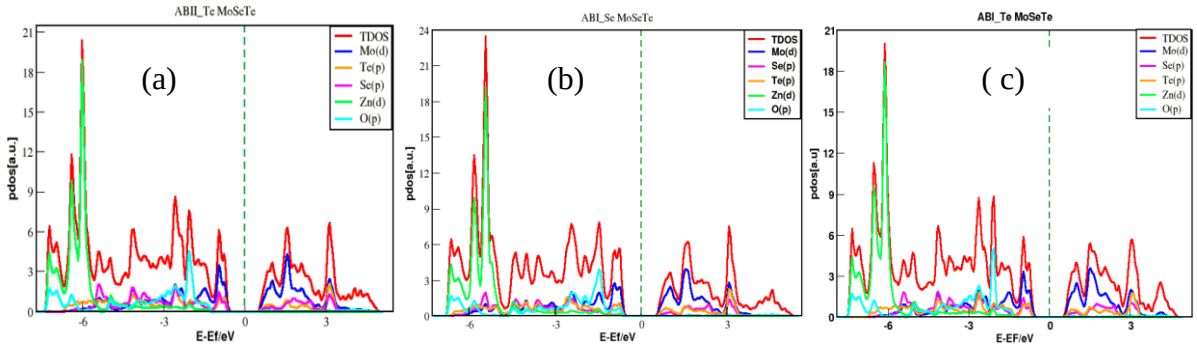


Figure 16: PDOS structure of the stacking pattern of ZnO/MoSeTe heterostructure.

## 4.8. ZnO/JTMDs HETROSTRUCTURE PHOTOCATALYST MATERIALS FOR WATER SPLITTING

One of the key prerequisites for water splitting is the conduction and valence band boundaries that span the reduction potential of hydrogen and the oxidation potential of water. In semiconductor photocatalyst materials, the levels of the conduction and valence bands, as well as the band gap width, are crucial parameters[58]. For photocatalytic water splitting to enable the simultaneous occurrence of both the hydrogen and oxygen evolution reactions, the band edges must align with the reduction and oxidation potential of water at a particular pH level[58].

The production of hydrogen using photocatalytic water splitting has drawn much attention due to its energy efficiency and environmental friendliness [88]. To enable the reduction and oxidation reactions to occur, a photocatalyst must possess a conduction band (CB) potential and valence band (VB) energy level that exceeds the potential of H+/H2 and OH-/O2, respectively[88]. In the process of complete water splitting, water molecules are oxidized by holes to produce O2, while

electrons reduce water molecules to form H2[96]. The standard redox potentials of water, in a vacuum, are 4.44 eV for reduction and 5.67 eV for oxidation[88].

Fig. 17 shows the band edge location of ABI-Se MoSeTe, ABI-Te MoSeTe, and ABII-Te MoSeTe heterostructures for water splitting. The stable stacking of ZnO-MoSeTe heterostructures has type II band alignment. This enhances the activity of photocatalytic water splitting and facilitates the efficient separation of charge carriers. The band edge locations of the heterostructures ABI-Se MoSeTe, ABI-Te MoSeTe, and ABII-Te MoSeTe do not align with the redox potentials of water at pH=0. As a result, the heterostructures do not effectively split water into hydrogen and oxygen molecules as required by thermodynamic theory. However, the heterostructures are a suitable photocatalyst for the HER as shown in Fig. 20(a). Several studies have shown that the band gap and band-edge locations of various semiconductor materials can be enhanced by applying strain. To utilize this heterostructure for complete water splitting, we will investigate the effect of strain on the conduction band edge.

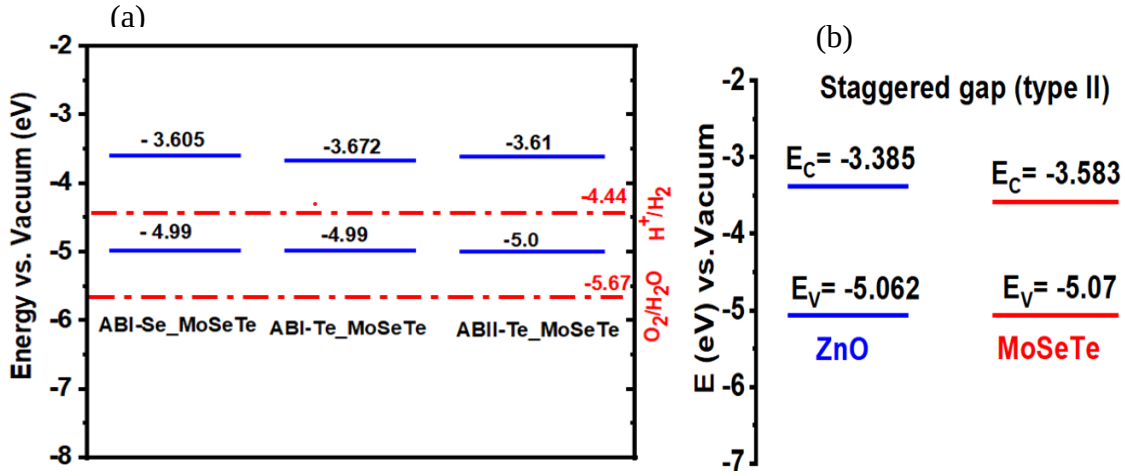


Figure 17 : (a) The positions of the band edges of the three ZnO-MoSeTe heterojunctions for photocatalytic water splitting. The broken red line represents the redox potential of water splitting at pH = 0. (b) Diagrammatic illustration of the type II band alignment ABII-Te MoSeTe heterostructure.

## 4.9. POWER CONVERSION EFFICIENCY(PCE) OF ZnO/MoSeTe HETROSTRUCTURES

PCE is the most significant characteristic of a photovoltaic device and is defined as the percentage of incident optical power Popt that is transformed into electricity with output power Pel[98]. The three stable configurations of the heterostructure being considered exhibit type-II band alignment

characteristics, which are crucial for photovoltaic energy conversion, as well as suitable band gaps, making them promising options for solar applications. The PCE of these heterostructures is calculated as the sum of the open-circuit voltage (VOC), short-circuit current (ISC), and fill factor (FF):

$$\text{PCE} = \frac{FFVocJsc}{P_{sun}} \quad (4.2)$$

Usinge $V_{OC} = E_g - E_{loss}$ (4.3)

$$J_{SC} = \int_E^{\infty} \frac{S(E)}{E} \text{dE} \quad (4.4)$$

$$P_{sun} = \int_0^{\infty} S(E)dE \quad (4.5)$$

where S(E) is the power supplied by the sun per unit area and photon energy, $V_{OC}$ is the open circuit voltage, E is the photon energy, Jsc is the short-circuit current (i.e., the current produced by all photons with energy greater than or equal to the band gap), and FF is the fill factor. The value of S(E) is determined using the NREL AM1.5 dataset. It is impossible to calculate the fill factor (FF) and energy losses (Eloss) from the first principles because they are empirical factors. A MoS2/p-Si heterostructure was reported to have a 0.57 fill factor in an earlier experimental investigation[99]. The fill factor we used in our analysis is based on the only known experimental investigation that provides a fill factor for a TMD. For energy loss ($E_{loss}$), we consider values of 0.2 and 0.3 [98,100]. The calculated power conversion efficiency (PCE) values for ABI-Se MoSeTe, ABI-Te MoSeTe, and ABII-Te MoSeTe are 22.26%, 22.31%, and 22.17% respectively, which are better than the MoS2/p-Si (5.23%)[101] and WSe2–MoS2 (2.56%)[102]results. As a result, our findings demonstrate that the band gaps of our materials are suitable and that they demonstrate type-II band alignment, making them a potentially attractive choice for use in solar cell applications.

# CHAPTER FIVE: CONCLUSION AND FUTURE WORK

## 5.1. CONCLUSION

This study uses a first principles DFT-based model to investigate the electronic properties of MoSeTe/ZnO vdW heterostructures, with a focus on their potential applications in solar cells and photocatalytic water splitting.

Eight different stacking modes in MoSeTe/ZnO heterostructures were examined to identify the more stable configuration depending on the binding energies and interlayer distance differences. Out of the eight stacking patterns considered, the most stable configurations for MoSeTe/ZnO are found to be ABI_Se, ABI_Te, and ABII_Te, each of which exhibits an indirect band gap. The band gap values for these configurations are 1.39 eV, 1.32 eV, and 1.39 eV, respectively. The band gap nature of three different stacking orders of vdW heterostructures exhibits almost the same gap nature with minor changes. Confirmation of the type II band alignment in these heterostructures has been obtained from the analysis of their electronic band structures. At interlayer layer spacings of 3.49 Å, 3.66 Å, and 3.64 Å, it is discovered that the binding energies of ABI_Se MoSeTe, ABI_Te MoSeTe, and ABII_Te MoSeTe heterostructures are 2.65 eV, 2.81 eV, and 2.97 eV respectively. The photocatalytic properties of these vdW heterostructures have been investigated in terms of their band edge alignment, with a focus on pH = 0 conditions. The results reveal that not all of these heterostructures meet the necessary band edge requirements for complete water splitting, they do exhibit favorable photocatalytic activity for the hydrogen evolution reaction when exposed to visible light. The Type-II ABI_Se MoSeTe, ABI_Te MoSeTe, and ABII_Se MoSeTe heterostructures show high solar PCEs at values of 22.26%, 22.31%, and 22.17%, respectively, and have excellent visible light absorption. The results demonstrate that the three stacking configurations of ZnO/MoSeTe heterostructures have great potential in photovoltaic applications.

## 5.2.FUTURE WORK

The MoSeTe/ZnO heterostructure study shows different interesting properties. The MoSeTe/ZnO heterostructure is computed by the PBE and HSE functional. To achieve improved electronic properties for fullness, it is recommended that future research should focus on studying the dynamic stabilities of these heterostructures. Different studies have demonstrated that the band gap and band-edge positions of semiconductor materials can be enhanced through the application of strain and doping techniques. In future studies, we recommend modulating the MoSeTe/ZnO heterostructure to demonstrate the effect of strain and doping to make this heterostructure possible for overall water splitting. Additionally, there are several chances to create novel 2D heterostructured materials with intriguing qualities that will make them attractive research materials in the future that will help companies and ultimately transform our society.

# REFERENCES


[1] A. Holt, I.J. Pengelly, ITS, and renewable energy," 15th World Congr. Intell. Transp, Syst. ITS Am. Annu. Meet. 6 (2008) 3854–3862. https://doi.org/10.1049/ic.2008.0789.

[2] N.L. Panwar, S.C. Kaushik, S. Kothari, Role of renewable energy sources in environmental protection: A review, Renew. Sustain. Energy Rev. 15 (2011) 1513–1524. https://doi.org/10.1016/j.rser.2010.11.037.

[3] A. Rawat, R. Ahammed, Dimple, N. Jena, M.K. Mohanta, A. De Sarkar, Solar Energy Harvesting in Type II van der Waals Heterostructures of Semiconducting Group III Monochalcogenide Monolayers, J. Phys. Chem. C. 123 (2019) 12666–12675. https://doi.org/10.1021/acs.jpcc.9b03359.

[4] T. Takata, C. Pan, K. Domen, Recent progress in oxynitride photocatalysts for visible-light-driven water splitting, Sci. Technol. Adv. Mater. 16 (2015) 33506. https://doi.org/10.1088/1468-6996/16/3/033506.

[5] Y. Khan, S.M. Obaidulla, M.R. Habib, A. Gayen, T. Liang, X. Wang, M. Xu, Recent breakthroughs in two-dimensional van der Waals magnetic materials and emerging applications, Nano Today. 34 (2020) 100902. https://doi.org/10.1016/j.nantod.2020.100902.

[6] J. Kegel, I.M. Povey, M.E. Pemble, Zinc oxide for solar water splitting: A brief review of the material's challenges and associated opportunities, Nano Energy. 54 (2018) 409–428. https://doi.org/10.1016/j.nanoen.2018.10.043.

[7] M. Ma, Y. Huang, J. Liu, K. Liu, Z. Wang, C. Zhao, S. Qu, Z. Wang, Engineering the photoelectrochemical behaviors of ZnO for efficient solar water splitting, J. Semicond. 41 (2020). https://doi.org/10.1088/1674-4926/41/9/091702.

[8] R.C. on E. Pollution, Novel Materials in the Environment : The case of nanotechnology Novel Materials in the Environment : The case of nanotechnology, 2008.

[9] K. S. Novoselov et al, Electric Field Effect in Atomically Thin Carbon Films, 306 (2016) 666–669.

[10] Y. Liu, R.F. Willis, K. V. Emtsev, T. Seyller, Plasmon dispersion and damping in electrically isolated two-dimensional charge sheets, Phys. Rev. B - Condens. Matter Mater. Phys. 78 (2008) 2–5. https://doi.org/10.1103/PhysRevB.78.201403.

[11] A. Betti, G. Fiori, G. Iannaccone, Strong mobility degradation in ideal graphene nanoribbons due to phonon scattering, Appl. Phys. Lett. 98 (2011). https://doi.org/10.1063/1.3587627.

[12] M.Q. Long, L. Tang, D. Wang, L. Wang, Z. Shuai, Theoretical predictions of size-dependent carrier mobility and polarity in graphene, J. Am. Chem. Soc. 131 (2009) 17728–17729. https://doi.org/10.1021/ja907528a.

[13] X. Wang, Y. Ouyang, X. Li, H. Wang, J. Guo, H. Dai, Room-temperature all-semiconducting sub-10-nm graphene nanoribbon field-effect transistors, Phys. Rev. Lett. 100 (2008) 100–103. https://doi.org/10.1103/PhysRevLett.100.206803.

[14] H. Zhang, Y.N. Zhang, H. Liu, L.M. Liu, Novel heterostructures by stacking layered molybdenum disulfides and nitrides for solar energy conversion, J. Mater. Chem. A. 2 (2014) 15389–15395. https://doi.org/10.1039/c4ta03134b.

[15] Y. Gong, H. Yuan, C.L. Wu, P. Tang, S.Z. Yang, A. Yang, G. Li, B. Liu, J. Van De Groep, M.L. Brongersma, M.F. Chisholm, S.C. Zhang, W. Zhou, Y. Cui, Spatially controlled doping of two-dimensional SnS2 through intercalation for electronics, Nat. Nanotechnol. 13 (2018) 294–299. https://doi.org/10.1038/s41565-018-0069-3.

[16] H.C. Yang, Y. Xie, J. Hou, A.K. Cheetham, V. Chen, S.B. Darling, Janus Membranes: Creating Asymmetry for Energy Efficiency, Adv. Mater. 30 (2018) 1–11. https://doi.org/10.1002/adma.201801495.
[17] M. Chhowalla, H.S. Shin, G. Eda, L.J. Li, K.P. Loh, H. Zhang, The chemistry of two-dimensional layered transition metal dichalcogenide nanosheets, Nat. Chem. 5 (2013) 263–275. https://doi.org/10.1038/nchem.1589.
[18] C. Ataca, H. Şahin, S. Ciraci, Stable, single-layer MX 2 transition-metal oxides and dichalcogenides in a honeycomb-like structure, J. Phys. Chem. C. 116 (2012) 8983–8999. https://doi.org/10.1021/jp212558p.
[19] Q. Xiang, J. Yu, M. Jaroniec, Synergetic E ff ect of MoS 2 and Graphene as Cocatalysts for Enhanced Photocatalytic H 2 Production Activity of TiO 2 Nanoparticles, (2012) 23–26.
[20] B. Radisavljevic, A. Kis, Mobility engineering and a metal-insulator transition in monolayer MoS2, Nat. Mater. 12 (2013) 815–820. https://doi.org/10.1038/nmat3687.
[21] T. Jin, J. Kang, E. Su Kim, S. Lee, C. Lee, Suspended single-layer MoS2 devices, J. Appl. Phys. 114 (2013) 0–4. https://doi.org/10.1063/1.4827477.
[22] L. Ju, M. Bie, X. Zhang, X. Chen, L. Kou, Two-dimensional Janus van der Waals heterojunctions: A review of recent research progresses, Front. Phys. 16 (2021) 169–175. https://doi.org/10.1007/s11467-020-1002-4.
[23] S. Najmaei, Z. Liu, W. Zhou, X. Zou, G. Shi, S. Lei, B.I. Yakobson, J.C. Idrobo, P.M. Ajayan, J. Lou, Vapour phase growth and grain boundary structure of molybdenum disulphide atomic layers, Nat. Mater. 12 (2013) 754–759. https://doi.org/10.1038/nmat3673.
[24] N. Huo, Y. Yang, Y. Wu, X. Zhang, S.T. Pantelides, G. Konstantatos, High carrier mobility in monolayer CVD-grown MoS2 through phonon suppression, (2018). https://doi.org/10.1039/c8nr04416c.
[25] Y. Cai, G. Zhang, Y. Zhang, Polarity-Reversed Robust Carrier Mobility in Monolayer MoS2 Nanoribbons, (2014).
[26] M. Yagmurcukardes, Y. Qin, S. Ozen, M. Sayyad, F.M. Peeters, S. Tongay, H. Sahin, Quantum properties and applications of 2D Janus crystals and their superlattices, Appl. Phys. Rev. 7 (2020). https://doi.org/10.1063/1.5135306.
[27] Y.C. Cheng, Z.Y. Zhu, M. Tahir, U. Schwingenschlögl, Spin-orbit-induced spin splittings in polar transition metal dichalcogenide monolayers, Epl. 102 (2013). https://doi.org/10.1209/0295-5075/102/57001.
[28] A.Y. Lu, H. Zhu, J. Xiao, C.P. Chuu, Y. Han, M.H. Chiu, C.C. Cheng, C.W. Yang, K.H. Wei, Y. Yang, Y. Wang, D. Sokaras, D. Nordlund, P. Yang, D.A. Muller, M.Y. Chou, X. Zhang, L.J. Li, Janus monolayers of transition metal dichalcogenides, Nat. Nanotechnol. 12 (2017) 744–749. https://doi.org/10.1038/nnano.2017.100.
[29] J. Zhang, S. Jia, I. Kholmanov, L. Dong, D. Er, W. Chen, H. Guo, Z. Jin, V.B. Shenoy, L. Shi, J. Lou, Janus Monolayer Transition-Metal Dichalcogenides, ACS Nano. 11 (2017) 8192–8198. https://doi.org/10.1021/acsnano.7b03186.
[30] R. Peng, Y. Ma, S. Zhang, B. Huang, Y. Dai, Valley Polarization in Janus Single-Layer MoSSe via Magnetic Doping, J. Phys. Chem. Lett. 9 (2018) 3612–3617. https://doi.org/10.1021/acs.jpclett.8b01625.
[31] W. Chen, E.J.G. Santos, W. Zhu, E. Kaxiras, Z. Zhang, Tuning the electronic and chemical properties of monolayer MoS2 adsorbed on transition metal substrates, Nano Lett. 13 (2013) 509–514. https://doi.org/10.1021/nl303909f.
[32] K.F. Mak, C. Lee, J. Hone, J. Shan, T.F. Heinz, Atomically thin MoS2: A new direct-gap

semiconductor, Phys. Rev. Lett. 105 (2010) 2–5. https://doi.org/10.1103/PhysRevLett.105.136805.
[33] S. Cahangirov, C. Ataca, M. Topsakal, H. Sahin, S. Ciraci, Frictional figures of merit for single layered nanostructures, Phys. Rev. Lett. 108 (2012) 1–5. https://doi.org/10.1103/PhysRevLett.108.126103.
[34] W.J. Yin, B. Wen, G.Z. Nie, X.L. Wei, L.M. Liu, Tunable dipole and carrier mobility for a few layer Janus MoSSe structure, J. Mater. Chem. C. 6 (2018) 1693–1700. https://doi.org/10.1039/c7tc05225a.
[35] H.C. Yang, J. Hou, V. Chen, Z.K. Xu, Janus Membranes: Exploring Duality for Advanced Separation, Angew. Chemie - Int. Ed. 55 (2016) 13398–13407. https://doi.org/10.1002/anie.201601589.
[36] Y. Guo, S. Zhou, Y. Bai, J. Zhao, Enhanced piezoelectric effect in Janus group-III chalcogenide monolayers, Appl. Phys. Lett. 110 (2017). https://doi.org/10.1063/1.4981877.
[37] X. Li, Z. Li, J. Yang, Proposed photosynthesis method for producing hydrogen from dissociated water molecules using incident near-infrared light, Phys. Rev. Lett. 112 (2014) 1–5. https://doi.org/10.1103/PhysRevLett.112.018301.
[38] K. Zhang, J.K. Kim, B. Park, S. Qian, B. Jin, X. Sheng, H. Zeng, H. Shin, S.H. Oh, C.L. Lee, J.H. Park, Defect-Induced Epitaxial Growth for Efficient Solar Hydrogen Production, Nano Lett. 17 (2017) 6676–6683. https://doi.org/10.1021/acs.nanolett.7b02622.
[39] X. Ma, X. Yong, C.C. Jian, J. Zhang, Transition Metal-Functionalized Janus MoSSe Monolayer: A Magnetic and Efficient Single-Atom Photocatalyst for Water-Splitting Applications, J. Phys. Chem. C. 123 (2019) 18347–18354. https://doi.org/10.1021/acs.jpcc.9b03003.
[40] Z. Guan, S. Ni, S. Hu, Tunable Electronic and Optical Properties of Monolayer and Multilayer Janus MoSSe as a Photocatalyst for Solar Water Splitting: A First-Principles Study, J. Phys. Chem. C. 122 (2018) 6209–6216. https://doi.org/10.1021/acs.jpcc.8b00257.
[41] Y. Ji, M. Yang, H. Lin, T. Hou, L. Wang, Y. Li, S.T. Lee, Janus Structures of Transition Metal Dichalcogenides as the Heterojunction Photocatalysts for Water Splitting, J. Phys. Chem. C. 122 (2018) 3123–3129. https://doi.org/10.1021/acs.jpcc.7b11584.
[42] R. Peng, Y. Ma, B. Huang, Y. Dai, Two-dimensional Janus PtSSe for photocatalytic water splitting under the visible or infrared light, J. Mater. Chem. A. 7 (2019) 603–610. https://doi.org/10.1039/c8ta09177c.
[43] C.F. Fu, J. Sun, Q. Luo, X. Li, W. Hu, J. Yang, Intrinsic Electric Fields in Two-dimensional Materials Boost the Solar-to-Hydrogen Efficiency for Photocatalytic Water Splitting, Nano Lett. 18 (2018) 6312–6317. https://doi.org/10.1021/acs.nanolett.8b02561.
[44] X.W. Zhao, B. Qiu, G.C. Hu, W.W. Yue, J.F. Ren, X.B. Yuan, Transition-metal doping/adsorption induced valley polarization in Janus WSSe: First-principles calculations, Appl. Surf. Sci. 490 (2019) 172–177. https://doi.org/10.1016/j.apsusc.2019.06.051.
[45] Y. Yang, Y. Zhang, H. Ye, Z. Yu, Y. Liu, B. Su, W. Xu, Structural and electronic properties of 2H phase Janus transition metal dichalcogenide bilayers, Superlattices Microstruct. 131 (2019) 8–14. https://doi.org/10.1016/j.spmi.2019.05.027.
[46] Y. Kang, S. Najmaei, Z. Liu, Y. Bao, Y. Wang, X. Zhu, N.J. Halas, P. Nordlander, P.M. Ajayan, J. Lou, Z. Fang, Plasmonic Hot Electron Induced Structural Phase Transition in a MoS2 Monolayer, Adv. Mater. 26 (2014) 6467–6471. https://doi.org/10.1002/adma.201401802.
[47] W.J. Yin, H.J. Tan, P.J. Ding, B. Wen, X.B. Li, G. Teobaldi, L.M. Liu, Recent advances in

low-dimensional Janus materials: Theoretical and simulation perspectives, Mater. Adv. 2 (2021) 7543–7558. https://doi.org/10.1039/d1ma00660f.
[48] D.B. Trivedi, G. Turgut, Y. Qin, M.Y. Sayyad, D. Hajra, M. Howell, L. Liu, S. Yang, N.H. Patoary, H. Li, M.M. Petrić, M. Meyer, M. Kremser, M. Barbone, G. Soavi, A. V. Stier, K. Müller, S. Yang, I.S. Esqueda, H. Zhuang, J.J. Finley, S. Tongay, Room-Temperature Synthesis of 2D Janus Crystals and their Heterostructures, Adv. Mater. 32 (2020) 1–9. https://doi.org/10.1002/adma.202006320.
[49] Y.C. Lin, C. Liu, Y. Yu, E. Zarkadoula, M. Yoon, A.A. Puretzky, L. Liang, X. Kong, Y. Gu, A. Strasser, H.M. Meyer, M. Lorenz, M.F. Chisholm, I.N. Ivanov, C.M. Rouleau, G. Duscher, K. Xiao, D.B. Geohegan, Low Energy Implantation into Transition-Metal Dichalcogenide Monolayers to Form Janus Structures, ACS Nano. 14 (2020) 3896–3906. https://doi.org/10.1021/acsnano.9b10196.
[50] J. Wang, H. Shu, T. Zhao, P. Liang, N. Wang, D. Cao, X. Chen, Intriguing electronic and optical properties of two-dimensional Janus transition metal dichalcogenides, Phys. Chem. Chem. Phys. 20 (2018) 18571–18578. https://doi.org/10.1039/c8cp02612b.
[51] C. Xia, W. Xiong, J. Du, T. Wang, Y. Peng, J. Li, Universality of electronic characteristics and photocatalyst applications in the two-dimensional Janus transition metal dichalcogenides, Phys. Rev. B. 98 (2018) 1–8. https://doi.org/10.1103/PhysRevB.98.165424.
[52] W. Zhou, J. Chen, Z. Yang, J. Liu, F. Ouyang, Geometry and electronic structure of monolayer, bilayer, and multilayer Janus WSSe, Phys. Rev. B. 99 (2019) 1–7. https://doi.org/10.1103/PhysRevB.99.075160.
[53] C. Shang, B. Xu, X. Lei, S. Yu, D. Chen, M. Wu, B. Sun, G. Liu, C. Ouyang, Bandgap tuning in MoSSe bilayers: Synergistic effects of dipole moment and interlayer distance, Phys. Chem. Chem. Phys. 20 (2018) 20919–20926. https://doi.org/10.1039/c8cp04208j.
[54] W.-J. Yin, H.-J. Tan, P.-J. Ding, B. Wen, X.-B. Li, G. Teobaldi, L.-M. Liu, Recent advances in low-dimensional Janus materials: theoretical and simulation perspectives, Mater. Adv. (2021). https://doi.org/10.1039/d1ma00660f.
[55] K. Zhang, Y. Guo, Q. Ji, A.Y. Lu, C. Su, H. Wang, A.A. Puretzky, D.B. Geohegan, X. Qian, S. Fang, E. Kaxiras, J. Kong, S. Huang, Enhancement of van der Waals Interlayer Coupling through Polar Janus MoSSe, J. Am. Chem. Soc. 142 (2020) 17499–17507. https://doi.org/10.1021/jacs.0c07051.
[56] F. Li, W. Wei, P. Zhao, B. Huang, Y. Dai, Electronic and Optical Properties of Pristine and Vertical and Lateral Heterostructures of Janus MoSSe and WSSe, J. Phys. Chem. Lett. 8 (2017) 5959–5965. https://doi.org/10.1021/acs.jpclett.7b02841.
[57] W. Yin, B. Wen, Q. Ge, D. Zou, Y. Xu, M. Liu, X. Wei, M. Chen, X. Fan, Role of intrinsic dipole on photocatalytic water splitting for Janus MoSSe/nitrides heterostructure: A first-principles study, Prog. Nat. Sci. Mater. Int. 29 (2019) 335–340. https://doi.org/10.1016/j.pnsc.2019.05.003.
[58] A. Rawat, M.K. Mohanta, N. Jena, Dimple, R. Ahammed, A. De Sarkar, Nanoscale Interfaces of Janus Monolayers of Transition Metal Dichalcogenides for 2D Photovoltaic and Piezoelectric Applications, J. Phys. Chem. C. 124 (2020) 10385–10397. https://doi.org/10.1021/acs.jpcc.0c02199.
[59] N. Zhao, U. Schwingenschlögl, Transition from Schottky to Ohmic contacts in Janus MoSSe/germanene heterostructures, Nanoscale. 12 (2020) 11448–11454. https://doi.org/10.1039/d0nr02084b.

[60] X. Liu, P. Gao, W. Hu, J. Yang, Photogenerated-Carrier Separation and Transfer in Two-Dimensional Janus Transition Metal Dichalcogenides and Graphene van der Waals Sandwich Heterojunction Photovoltaic Cells, J. Phys. Chem. Lett. 11 (2020) 4070–4079. https://doi.org/10.1021/acs.jpclett.0c00706.
[61] X. Zhang, Y. Cui, L. Sun, M. Li, J. Du, Y. Huang, Stabilities, and electronic and piezoelectric properties of two-dimensional tin dichalcogenide derived Janus monolayers, J. Mater. Chem. C. 7 (2019) 13203–13210. https://doi.org/10.1039/c9tc04461b.
[62] X. Tang, S. Li, Y. Ma, A. Du, T. Liao, Y. Gu, L. Kou, Distorted Janus Transition Metal Dichalcogenides: Stable Two-Dimensional Materials with Sizable Band Gap and Ultrahigh Carrier Mobility, J. Phys. Chem. C. 122 (2018) 19153–19160. https://doi.org/10.1021/acs.jpcc.8b04161.
[63] Y. Sun, Z. Shuai, D. Wang, Janus monolayer of WSeTe, a new structural phase transition material driven by electrostatic gating, Nanoscale. 10 (2018) 21629–21633. https://doi.org/10.1039/c8nr08151d.
[64] Y. Bai, Q. Zhang, N. Xu, K. Deng, E. Kan, The Janus structures of group-III chalcogenide monolayers as promising photocatalysts for water splitting, Appl. Surf. Sci. 478 (2019) 522–531. https://doi.org/10.1016/j.apsusc.2019.02.004.
[65] L. Ye, Y. Xiong, M. Zhang, X. Guo, H. Guan, Y. Zou, H. Ade, Enhanced efficiency in nonfullerene organic solar cells by tuning molecular order and domain characteristics, Nano Energy. 77 (2020) 105310. https://doi.org/10.1016/j.nanoen.2020.105310.
[66] S.P. Kaur, T.J. Dhilip Kumar, Tuning structure, electronic, and catalytic properties of non-metal atom doped Janus transition metal dichalcogenides for hydrogen evolution, Appl. Surf. Sci. 552 (2021) 149146. https://doi.org/10.1016/j.apsusc.2021.149146.
[67] F. Ersan, F. Ersan, C. Ataca, Janus Pt XnY2-n (X, y = S, Se, Te; $0 \leq n \leq 2$) Monolayers for Enhanced Photocatalytic Water Splitting, Phys. Rev. Appl. 13 (2020) 1. https://doi.org/10.1103/PhysRevApplied.13.064008.
[68] X. Ma, X. Wu, H. Wang, Y. Wang, A Janus MoSSe monolayer: A potential wide solar-spectrum water-splitting photocatalyst with a low carrier recombination rate, J. Mater. Chem. A. 6 (2018) 2295–2301. https://doi.org/10.1039/c7ta10015a.
[69] F. Paquin, J. Rivnay, A. Salleo, N. Stingelin, C. Silva-Acuña, Multi-phase microstructures drive exciton dissociation in neat semicrystalline polymeric semiconductors, J. Mater. Chem. C. 3 (2015) 10715–10722. https://doi.org/10.1039/c5tc02043c.
[70] W. Yin, B. Wen, Q. Ge, D. Zou, Y. Xu, M. Liu, X. Wei, M. Chen, X. Fan, Progress in Natural Science : Materials International Role of the intrinsic dipole on photocatalytic water splitting for Janus MoSSe / nitrides heterostructure : A first-principles study, Prog. Nat. Sci. Mater. Int. 29 (2019) 335–340. https://doi.org/10.1016/j.pnsc.2019.05.003.
[71] T. Zheng, Y.C. Lin, Y. Yu, P. Valencia-Acuna, A.A. Puretzky, R. Torsi, C. Liu, I.N. Ivanov, G. Duscher, D.B. Geohegan, Z. Ni, K. Xiao, H. Zhao, Excitonic Dynamics in Janus MoSSe and WSSe Monolayers, Nano Lett. 21 (2021) 931–937. https://doi.org/10.1021/acs.nanolett.0c03412.
[72] P. Giannozzi, S. Baroni, N. Bonini, M. Calandra, R. Car, C. Cavazzoni, D. Ceresoli, G.L. Chiarotti, M. Cococcioni, I. Dabo, A. Dal Corso, S. De Gironcoli, S. Fabris, G. Fratesi, R. Gebauer, U. Gerstmann, C. Gougoussis, A. Kokalj, M. Lazzeri, L. Martin-Samos, N. Marzari, F. Mauri, R. Mazzarello, S. Paolini, A. Pasquarello, L. Paulatto, C. Sbraccia, S. Scandolo, G. Sclauzero, A.P. Seitsonen, A. Smogunov, P. Umari, R.M. Wentzcovitch, QUANTUM ESPRESSO: A modular and open-source software project for quantum

simulations of materials, J. Phys. Condens. Matter. 21 (2009). https://doi.org/10.1088/0953-8984/21/39/395502.
[73] Y.S. Meng, M.E. Arroyo-De Dompablo, First-principles computational materials design for energy storage materials in lithium-ion batteries, Energy Environ. Sci. 2 (2009) 589.
[74] P. A, Z. V.A, B. L.L, A multiple-item scale for measuring consumer perceptions of service quality, J. Retail. 64 (1998) 12–40.
[75] N. Carolina, P.G. Cook, P.G.E. Matthews, P.K.D. Bonin, Computational Research on Lithium Ion Battery Materials, 2006.
[76] K. Hohenberg, Inhomogeneous Electron Gas, Phys. Rev. 155 (1964) B864–B871.
[77] Kohn W. Sham L. J., Self-Consistent Equations Including Exchange and Correlation Effects, Phys. Rev. 140 (1965) A1133–A1138.
[78] A. Hossain, Introduction to density functional theory, 1 (2004) 1–7. https://doi.org/10.1007/s00214-013-1372-6.
[79] J. Carmona-espíndola, J.L. Gázquez, A. Vela, S.B. Trickey, Generalized gradient approximation exchange energy functional with the correct asymptotic behavior of the corresponding potential, Phys. Rev. (2012) 1–40.
[80] J. Perdew, J. Chevary, S. Vosko, K. Jackson, M. Pederson, D. Singh, C. Fiolhais, Atoms, molecules, solids, and surfaces: Applications of the generalized gradient approximation for exchange and correlation, Phys. Rev. B. 46 (1992) 6671–6687. https://doi.org/10.1103/PhysRevB.48.4978.2.
[81] J.P. Perdew, K. Burke, M. Ernzerhof, Generalized gradient approximation made simple, Phys. Rev. Lett. 77 (1996) 3865–3868. https://doi.org/10.1103/PhysRevLett.77.3865.
[82] B. Hammer, L.B. Hansen, J.K. Nørskov, Improved adsorption energetics within density-functional theory using revised Perdew-Burke-Ernzerhof functionals, Phys. Rev. B. 59 (1999) 7413–7421. https://doi.org/10.1103/PhysRevB.59.7413.
[83] G. Román-Pérez, J.M. Soler, Efficient implementation of a van der Waals density functional: Application to double-wall carbon nanotubes, Phys. Rev. Lett. 103 (2009) 1–4. https://doi.org/10.1103/PhysRevLett.103.096102.
[84] A.D. Becke, Density-functional thermochemistry. III. The role of exact exchange, J. Chem. Phys. 98 (1993) 5648–5652. https://doi.org/10.1063/1.464913.
[85] J. Paier, M. Marsman, K. Hummer, G. Kresse, I.C. Gerber, J.G. Angyán, Screened hybrid density functionals applied to solids, J. Chem. Phys. 124 (2006). https://doi.org/10.1063/1.2187006.
[86] J. Paier, M. Marsman, G. Kresse, Why does the B3LYP hybrid functional fail for metals?, J. Chem. Phys. 127 (2007). https://doi.org/10.1063/1.2747249.
[87] E.A. Peterson, T.T. Debela, G.M. Gomoro, J.B. Neaton, G.A. Asres, Electronic structure of strain-tunable Janus WSSe-ZnO heterostructures from first-principles, RSC Adv. 12 (2022) 31303–31316. https://doi.org/10.1039/d2ra05533c.
[88] B.T. Beshir, K.O. Obodo, Janus transition metal dichalcogenides in combination with MoS 2 for high-e ffi ciency photovoltaic applications : a DFT study †, (2022) 13749–13755. https://doi.org/10.1039/d2ra00775d.
[89] S. Saini, A. Shrivastava, A. Dixit, S. Singh, Ultra-low lattice thermal conductivity and high figure of merit for Janus MoSeTe monolayer: a peerless material for high temperature regime thermoelectric devices, J. Mater. Sci. 57 (2022) 7012–7022. https://doi.org/10.1007/s10853-022-07065-3.
[90] P.D. Thesis, The electronic structure of perfect and defective perovskite crystals : Ab initio,

(2003).
[91] K. Ren, J. Yu, W. Tang, Two-dimensional ZnO/BSe van der Waals heterostructure used as a promising photocatalyst for water splitting: A DFT study, J. Alloys Compd. 812 (2020) 152049. https://doi.org/10.1016/j.jallcom.2019.152049.
[92] A.A. Mohamad, M.S. Hassan, M.K. Yaakob, M.F.M. Taib, F.W. Badrudin, O.H. Hassan, M.Z.A. Yahya, First-principles calculation on electronic properties of zinc oxide by zinc–air system, J. King Saud Univ. - Eng. Sci. 29 (2017) 278–283. https://doi.org/10.1016/j.jksues.2015.08.002.
[93] X. Yang, D. Singh, Z. Xu, Z. Wang, R. Ahuja, An emerging Janus MoSeTe material for potential applications in optoelectronic devices, J. Mater. Chem. C. 7 (2019) 12312–12320. https://doi.org/10.1039/c9tc03936h.
[94] A. Manuscript, rsc.li/pccp, 19 (2020). https://doi.org/10.1039/D0CP01264E.
[95] X. Li, L. Wu, S. Cheng, C. Chen, P. Lu, First-principles study on optoelectronic properties of Cs2PbX4-PtSe2van der Waals heterostructures, RSC Adv. 12 (2022) 2292–2299. https://doi.org/10.1039/d1ra08574c.
[96] S.T. Ayele, K.O. Obodo, G.A. Asres, First-principles investigation of potential water-splitting photocatalysts and photovoltaic materials based on Janus transition-metal dichalcogenide/WSe2 heterostructures, RSC Adv. 12 (2022) 31518–31524. https://doi.org/10.1039/d2ra04964c.
[97] S. Wang, C. Ren, H. Tian, J. Yu, M. Sun, MoS2/ZnO van der Waals heterostructure as a high-efficiency water splitting photocatalyst: A first-principles study, Phys. Chem. Chem. Phys. 20 (2018) 13394–13399. https://doi.org/10.1039/c8cp00808f.
[98] M.M. Furchi, F. Höller, L. Dobusch, D.K. Polyushkin, S. Schuler, T. Mueller, Device physics of van der Waals heterojunction solar cells, Npj 2D Mater. Appl. 2 (2018) 1–7. https://doi.org/10.1038/s41699-018-0049-3.
[99] S.K. Pradhan, B. Xiao, A.K. Pradhan, Enhanced photo-response in p-Si/MoS2 heterojunction-based solar cells, Sol. Energy Mater. Sol. Cells. 144 (2016) 117–127. https://doi.org/10.1016/j.solmat.2015.08.021.
[100] K. Lai, C.L. Yan, L.Q. Gao, W.B. Zhang, AI3 (A = As, Sb) Single Layers and Their vdW Heterostructure for Photocatalysis and Solar Cell Applications, J. Phys. Chem. C. 122 (2018) 7656–7663. https://doi.org/10.1021/acs.jpcc.8b01874.
[101] M. Tsai, S. Su, J. Chang, D. Tsai, C. Chen, C. Wu, L. Li, L. Chen, J. He, M. Science, E. Engineering, M. Sciences, M. Sciences, S. Arabia, Monolayer MoS 2 Heterojunction Solar, ACS Nano. 8 (2014) 8317–8322.
[102] M.L. Tsai, M.Y. Li, J.R.D. Retamal, K.T. Lam, Y.C. Lin, K. Suenaga, L.J. Chen, G. Liang, L.J. Li, J.H. He, Single Atomically Sharp Lateral Monolayer p-n Heterojunction Solar Cells with Extraordinarily High Power Conversion Efficiency, Adv. Mater. 29 (2017) 1–7. https://doi.org/10.1002/adma.201701168.